CANCER

Single-cell protein activity analysis reveals aberrant myogenesis and IGF2-PI3K pathway dependencies in *MYOD1*-mutant rhabdomyosarcoma

Josephine K. Dermawan[1], Fabio Vanoli[2], Henry de Traux de Wardin[3], Jonathan N. Levi[4], Glorymar Ibanez Sanchez[5], Armaan Siddiquee[5], Samantha Brosius[5], Daoqi You[5], Franck Tirode[6], Patricia Sung[2], Marie Karanian[6], Daniel Pissaloux[6], Leonard H. Wexler[5], Andrew Kung[5], Alice Soragni[4], Filemon S. Dela Cruz[5], Jovana Pavisic[5]*, Cristina R. Antonescu[2]*

Myogenic differentiation 1 *(MYOD1)*^{L122R}-mutant spindle cell rhabdomyosarcoma (SRMS) is an ultrarare, treatment-resistant sarcoma with dismal outcomes. We performed regulatory network analysis of single-nucleus RNA sequencing (snRNA-seq) from six patient tumors, revealing disrupted myogenesis and actionable master regulator (MR) dependencies across three coexisting tumor cell states, also conserved in patient-derived xenografts: (i) a MYOD1-enriched progenitor-like state, (ii) a proliferative transition state, and (iii) a partially differentiated state with reduced MYOD1 activity. Ligand-receptor analysis uncovered paracrine insulin-like growth factor 2 (IGF2)-IGF1 receptor (IGF1R)–phosphatidylinositol 3-kinase (PI3K) signaling from progenitor to transition/differentiated states, whose inhibition demonstrated therapeutic potential in ex vivo drug screens, and significantly improved disease control in a patient-derived xenograft model. Oncogenic MRs were recapitulated in 24 bulk RNA profiles, while 20 DNA profiles revealed recurrent IGF2/PI3K/AKT alterations, reinforcing shared transcriptional vulnerabilities. These findings characterize aberrant, mutant MYOD1–driven myogenesis sustained by IGF2 and nominate IGF1R-PI3K/AKT/mammalian target of rapamycin inhibitors for therapeutic translation in *MYOD1*^{L122R}-mutant SRMS, underscoring the utility of single-cell regulatory network analysis for uncovering actionable dependencies in rare, transcriptionally complex cancers.

INTRODUCTION

MYOD1-mutant spindle cell/sclerosing rhabdomyosarcoma (SRMS) is an ultrarare and clinically aggressive soft tissue sarcoma that primarily affects children and young adults, with dismal outcomes (*1*–*4*). It is defined by a recurrent Leu122Arg (L122R) hotspot mutation in the myogenic differentiation 1 (*MYOD1*) gene that disrupts the normal function of this key transcription factor in skeletal muscle differentiation (*5*, *6*). The disease exhibits poor responsiveness to conventional chemotherapy, with limited durable responses, high rates of relapse, and less than 20% 5-year survival (*7*, *8*). While the defining mutation is well characterized, the regulatory programs that sustain tumor progression, intratumor heterogeneity, and therapy resistance remain poorly understood. Long-term survival is rare, and effective targeted therapies are lacking—underscoring the need for previously unexplored, mechanistically informed treatment strategies.

Pediatric cancers typically exhibit a low mutational burden yet show substantial transcriptional and cellular heterogeneity that critically influences tumor behavior (*9*, *10*). In *MYOD1*^{L122R}-mutant SRMS, 30 to 40% of tumors harbor recurrent, potentially actionable comutations, frequently involving the phosphatidylinositol 3-kinase (PI3K)/AKT/mammalian target of rapamycin (mTOR) pathway—most commonly *PIK3CA* hotspot mutations (*2*–*4*, *10*–*12*). However, the absence of actionable mutations in many tumors and unclear functional relevance of observed alterations hinder efforts to identify therapeutic targets through genomics alone. Despite this, the transcriptional programs that define cell states and regulatory dependencies in *MYOD1*^{L122R}-mutant SRMS have yet to be systematically characterized.

Recent single-cell RNA sequencing (scRNA-seq) studies in fusion-positive RMS (*FOXO1*-rearranged; FP-RMS) and fusion-negative RMS (FN-RMS) have revealed complex intratumor heterogeneity reflective of myogenic developmental hierarchies, with therapeutic implications (*13*–*16*). *MYOD1*^{L122R}-mutant SRMS, however, has been largely excluded from these efforts, with only two cases profiled to date. Unlike the primitive small round blue cell and spindled histology seen in FP-RMS and FN-RMS, this subtype is morphologically and molecularly unique, exhibiting a fascicular, spindled, and sclerosing cytomorphology, along with focal myogenin (MYOG) expression (*3*). Moreover, *MYOD1*^{L122R} has been shown to interfere with normal skeletal muscle differentiation, leading to reprogramming and arrest of myogenic maturation (*5*, *6*). Together, these features suggest that *MYOD1*^{L122R}-mutant SRMS likely exhibits divergent developmental and transcriptional programs requiring further study.

To address this gap, we performed single-nucleus RNA sequencing (snRNA-seq) on patient-derived *MYOD1*^{L122R}-mutant SRMS tumors. This was complemented by bulk RNA-seq and targeted DNA sequencing to generate one of the most comprehensive molecular characterizations to date in this rare sarcoma. We used an extensively validated regulatory network–based approach (*17*–*23*) to identify regulatory drivers—master regulators (MRs)—of the cell

[1]Department of Pathology and Laboratory Medicine, Cleveland Clinic, Cleveland, OH, USA. [2]Department of Pathology and Laboratory Medicine, Memorial Sloan Kettering Cancer Center, New York, NY, USA. [3]Department of Pediatrics, Brussels University Hospital, Academic Children's Hospital Queen Fabiola, Université Libre de Bruxelles, Brussels, Belgium. [4]Department of Orthopaedic Surgery, David Geffen School of Medicine, University of California, Los Angeles, CA, USA. [5]Department of Pediatrics, Memorial Sloan Kettering Cancer Center, New York, NY, USA. [6]Cancer Research Center of Lyon, CNRS 5286, INSERM U1052, Department of Biopathology, Centre Léon Bérard, Université Claude Bernard Lyon 1, Lyon, France.
*Corresponding author. Email: pavisij1@mskcc.org (J.P.); antonesc@mskcc.org (C.R.A.)

states that comprise these tumors. Using a single-cell adaptation of the VIPER (Virtual Inference of Protein Activity by Enriched Regulon analysis) (*24*) algorithm (metaVIPER) (*25*), we inferred activity of transcriptional regulators and signaling proteins from the differential expression of their inferred context-specific regulatory targets (*24*–*27*). This enabled robust detection of critical regulators, including those with undetected transcripts in sparse snRNA-seq data, supporting deeper cell state characterization in the context of an ultrarare tumor with small sample size (*22*, *23*, *28*). Furthermore, MR proteins are enriched in tumor-essential genes and synthetic lethality candidates, thus representing actionable non-oncogene dependencies for therapeutic targeting (*18*, *20*, *21*, *23*, *29*, *30*).

This analysis revealed three distinct cell states coexisting in virtually all *MYOD1*^{L122R}-mutant SRMS tumors, reflecting mutant MYOD1–driven disruption of normal myogenic differentiation. This included a progenitor-like state, relatively enriched for MYOD1 activity. A progenitor-to-differentiated paracrine insulin-like growth factor 2 (IGF2)–IGF1 receptor (IGF1R) signaling axis emerged as a conserved driver of PI3K/AKT/mTOR activity sustaining the transition and differentiated states. MR dependencies were validated in an independent bulk RNA-seq cohort. Functional validation in chemotherapy-resistant patient-derived xenograft (PDX) cell cultures and organoids (PDXOs) demonstrated selective sensitivity to IGF1R and PI3K/AKT/mTOR pathway inhibitors. Critically, in vivo testing of a PI3K/mTOR inhibitor achieved meaningful disease control, and its combination with chemotherapy produced objective tumor regression, highlighting the translational potential of this strategy. Additional cell state–specific MRs were nominated as targets for rational combination therapy. These findings underscore a regulatory network–based framework for uncovering actionable dependencies in rare, heterogeneous cancers. They reveal that MYOD1-driven disruption of myogenic differentiation shapes a distinct transcriptional cell state architecture in *MYOD1*^{L122R}-mutant SRMS and advance mechanistically informed, functionally validated therapies for preclinical and clinical translation in this aggressive disease.

RESULTS

Single-nucleus transcriptomic landscape of *MYOD1*^{L122R}-mutant SRMS

Although intratumor heterogeneity and developmental hierarchies have been characterized in RMS broadly, *MYOD1*^{L122R}-mutant SRMS—a molecularly and clinically distinct entity—remains underrepresented in such analyses. However, the *MYOD1*^{L122R} mutation is known to disrupt normal skeletal muscle differentiation (*5*, *6*), likely driving unique transcriptional and developmental programs with potential therapeutic implications. To better characterize the intratumor heterogeneity and transcriptional regulatory programs in *MYOD1*^{L122R}-mutant SRMS, we performed snRNA-seq on six chemotherapy-exposed, patient-derived, snap-frozen *MYOD1*^{L122R}-mutant SRMS tumors (Fig. 1, A and B; Table 1; fig. S1, A and B; and table S1). To distinguish tumor from nontumor nuclei, we assessed single-nucleus somatic copy number alterations using InferCNV (*31*), comparing candidate tumor populations to sample-matched immune cells annotated by singleR (*32*). This defined a transformed tumor compartment in each sample marked by large-scale copy number alterations (Fig. 1C). Malignant nuclei constituted the predominant population (92% of the entire dataset), with nonmalignant stromal and immune cells representing 6 to 27% of total cells across samples. After filtering out nonmalignant cells from the immune (lymphoid and myeloid) and stromal compartments, the integrated *MYOD1*^{L122R}-mutant SRMS snRNA-seq dataset contained 177,051 high-quality malignant nuclei. This represents the largest single-cell transcriptomic dataset generated to date for this rare sarcoma subtype.

Clinical characteristics and treatment response of the *MYOD1*^{L122R}-mutant SRMS cohort

To contextualize the snRNA-seq findings, we reviewed the clinicopathologic features and treatment details for the six patients with *MYOD1*^{L122R}-mutant SRMS included in this analysis (Table 1, fig. S1A, and table S2). This clinically well-characterized cohort spans a wide age range (7 to 76 years; median: 35.5 years) and includes five males and one female. Sampled tumor size varied from 2.4 to 24 cm with three lower extremity, two pelvic, and one mediastinal tumor (Table 1). Four samples were additionally profiled by MSK-IMPACT (a targeted 341–505 gene matched tumor-normal DNA sequencing panel) (*33*). The variant allele frequency (VAF) of *MYOD1* was greater than 60% in these samples, consistent with either homozygosity of the mutant *MYOD1*^{L122R} allele or increased mutant allele burden due to chromosome 11p aneuploidy, together with heterogeneous co-occurring genomic alterations (table S2). All patients received neoadjuvant chemotherapy—most commonly 2 to 3 months of vincristine, actinomycin-D (dactinomycin), and cyclophosphamide (VAC)—followed by delayed surgical resection and adjuvant chemotherapy, with or without radiation therapy (fig. S1A).

Tumor tissue for snRNA-seq was obtained from the primary site at initial surgical resection following neoadjuvant chemotherapy in four patients and during the first relapse in two patients (fig. S1A). Histopathologic assessment of post–neoadjuvant chemotherapy specimens revealed heterogeneous treatment responses. Two tumors, including the smallest tumor, demonstrated partial responses characterized by 50 to 60% fibrosis and therapy-induced cytodifferentiation, respectively; both patients remain alive with no evidence of disease at last follow-up (36 months from initial diagnosis). In contrast, four patients showed minimal to no histologic response to neoadjuvant chemotherapy, including the two largest tumors and two tumors sampled during first relapse. Posttreatment specimens from these cases contained viable hyperchromatic spindle cells arranged in fascicles or within sclerotic stroma, with minimal evidence of treatment effect (Fig. 1B). All four patients experienced disease progression and three subsequently died of their disease. By immunohistochemistry, MYOD1 was diffusely and strongly positive in all the samples, while myogenin was rare to negative (Fig. 1B and fig. S1C).

Single-cell protein activity analysis reveals cell state–specific regulatory programs and altered myogenic differentiation trajectories in *MYOD1*^{L122R}-mutant SRMS

To define the transcriptional regulatory architecture underlying intratumor heterogeneity in *MYOD1*^{L122R}-mutant SRMS, we applied a regulatory network–based framework for inferring protein activity from single-cell gene expression data (*25*–*27*). Using ARACNe-AP (Algorithm for the Reconstruction of Accurate Cellular Networks with Adaptive Partitioning), we first constructed sample-specific single-cell gene regulatory networks from tumor cell gene expression data across the six *MYOD1*^{L122R}-mutant SRMS. Tumor-specific regulatory interactions between candidate transcriptional regulators and their target genes (i.e., regulons) are reconstructed de novo and thus reflect context-dependent DNA binding alterations such as

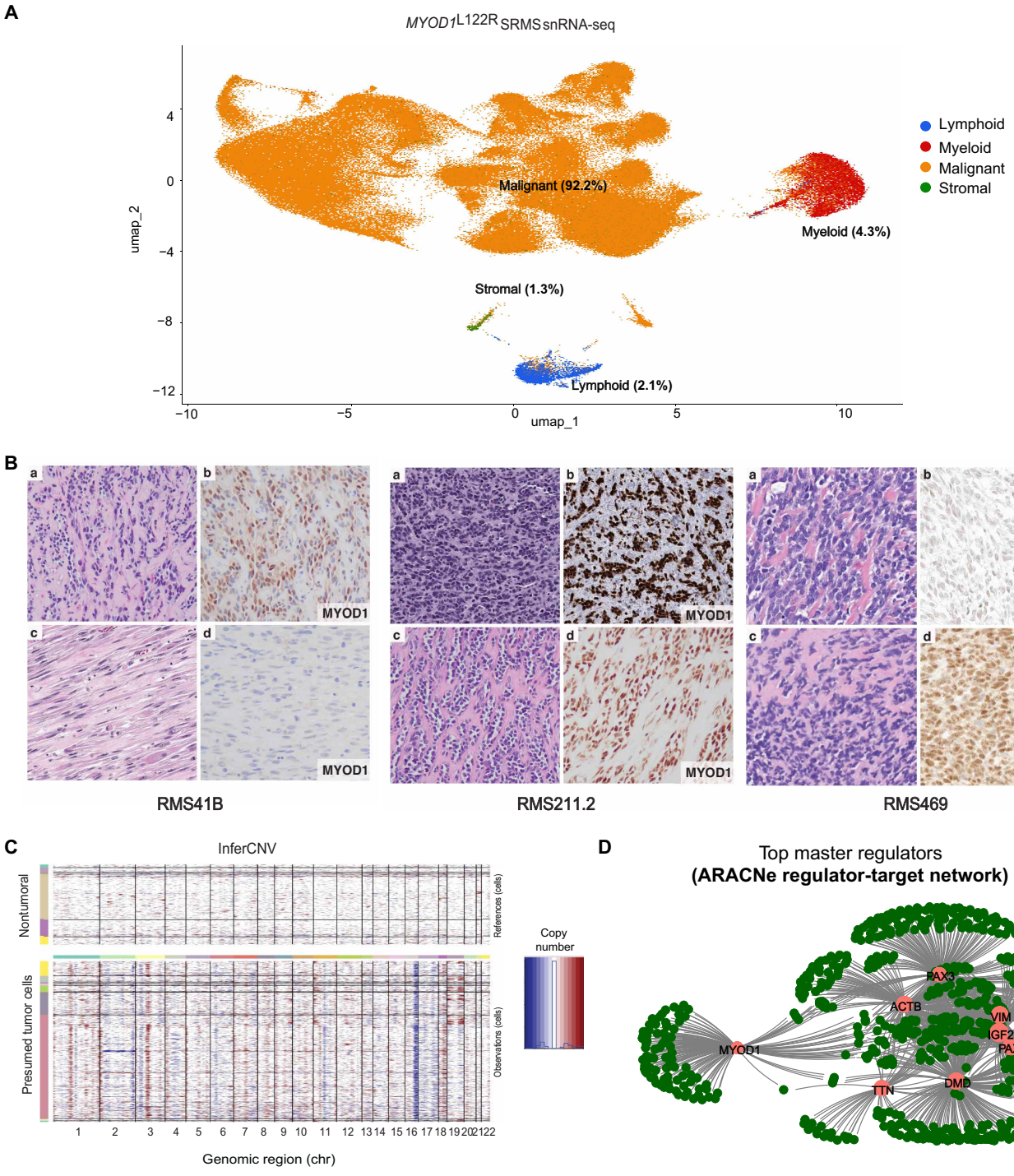

Fig. 1. Single-nucleus profiling of *MYOD1*^{L122R}-mutant SRMS and regulatory network inference. (**A**) Uniform manifold approximation and projection (UMAP) embedding of snRNA-seq gene expression profiles across six *MYOD1*^{L122R}-mutant SRMS tumors, annotated as malignant (tumoral) versus nonmalignant (nontumoral) using singleR. The integrated dataset includes 177,051 malignant nuclei. (**B**) Representative histomorphology (hematoxylin and eosin) and corresponding MYOD1 immunohistochemistry from paired pretreatment biopsies (a and b) and posttreatment resections (c and d) in three patients (RMS41B, RMS211.2, and RMS469). In RMS41B, posttreatment samples exhibited cytodifferentiation (i.e., skeletal muscle maturation), with transformation from poorly differentiated hyperchromatic spindle cells with scant cytoplasm to cells with abundant brightly eosinophilic myofilament-like cytoplasmic processes and loss of MYOD1 expression. (**C**) InferCNV heatmap of a representative tumor (RMS469), showing large-scale chromosomal copy number alterations (gains in red and losses in blue), confirming the transformed nature of presumed tumor single nuclei (rows), which are grouped by unsupervised gene expression clusters. Columns represent genomic regions across chromosomes; nonmalignant immune clusters were used as a reference. (**D**) Representative subnetwork of the ARACNe (Algorithm for the Reconstruction of Accurate Cellular Networks)–inferred *MYOD1*^{L122R}-mutant SRMS single-cell gene regulatory network, illustrating regulatory interactions between highly activated tumor MRs associated with myogenic differentiation and cytoskeletal organization, and their transcriptional targets.

Table 1. Clinical summary of six *MYOD1*^{L122R}-mutant SRMS with snRNA-seq profiling.

Case	Age	Sex	Primary site	Greatest dimension (cm)	Progression	Outcome
RMS475	35	M	Lower extremity	2.9	N/A	NED
RMS41B	40	M	Lower extremity	9.2	N/A	NED
RMS31.2	76	M	Lower extremity	19	Lung metastasis	DOD
RMS469	36	M	Mediastinum	24	Lung metastasis	AWD
RMS211.2	7	F	Pelvis	8.5	Local recurrence, soft tissue metastasis	DOD
RMS3.2	11	M	Pelvis	13.5	Local recurrence, lung metastasis	DOD

AWD, alive with disease; NED, alive with no evidence of disease; DOD, died of disease; M, male; F, female.

those induced by the *MYOD1*^{L122R} mutation. A representative subset of the inferred network illustrates both shared and divergent regulatory interactions among key regulators of myogenic differentiation and cytoskeletal organization. MYOD1 displayed a largely distinct target profile relative to other myogenic factors, consistent with altered regulatory function in the context of the L122R mutation (Fig. 1D). While ARACNe-AP cannot explicitly separate the contribution of mutant versus wild-type *MYOD1* expression, the high *MYOD1* VAF across samples suggests that the inferred MYOD1 regulon largely reflects mutant-driven activity, although some contribution of wild-type MYOD1 in the context of chromosome 11p aneuploidy cannot be excluded.

We then used metaVIPER to infer the activity of 2336 regulatory proteins in each cell based on the differential expression of their target genes in sample-specific, internally scaled tumor gene expression profiles, transforming sparse gene expression data into dense, robust protein activity signatures (table S3 and S4). A schematic overview of the analysis is shown in Fig. 2, summarizing the workflow from de novo regulon construction and protein activity inference to subsequent characterization of tumor cell states and functional validation of their regulatory dependencies described below.

First, unsupervised clustering of tumor cells by metaVIPER-inferred protein activity (resolution-optimized Louvain algorithm; see Materials and Methods) identified 20 patient-specific subclusters across the six *MYOD1*^{L122R}-mutant SRMS tumors (two to five clusters per tumor; Figs. 2 and 3, A and B, and fig. S1D). To define consensus transcriptional states, we then assessed pairwise similarity among subcluster mean protein activity signatures using viperSimilarity, which quantifies overlap in shared MR protein activities by analytic rank–based enrichment analysis [aREA (*24*)] (Fig. 3C). Hierarchical clustering of the viperSimilarity matrix revealed three broadly defined groups of subclusters with concordant MR activity profiles that lay along a continuum of differentiation rather than forming discrete cell states. Among subclusters with significantly conserved MR activity profiles, final cell state assignments were thus further refined on the basis of similarity in differentiation potential and lineage features, including CytoTRACE-inferred differentiation potential (*34*), proliferative fraction (Seurat S and G2/M scores), and metaVIPER-inferred activity of canonical myogenic regulators (Fig. 3, D to F, and fig. S2, A to C). On the basis of concordant patterns across these features, subclusters were consolidated into three functionally distinct tumor-derived cell states with unique MR profiles that were consistently observed across patients: progenitor (68,265 nuclei), transition (82,053 nuclei), and differentiated (26,292 nuclei) (Figs. 2 and 3, A to G, and figs. S1D and S2, A to C).

Together, these data reveal a cell state architecture with disrupted myogenic differentiation in *MYOD1*^{L122R}-mutant SRMS. The progenitor state, comprising the least differentiated tumor cells by CytoTRACE, was marked by significant enrichment of a mesenchymal stem cell gene signature and absence of canonical myogenic transcription factor activity (Fig. 3, D, F, and G, and fig. S2, B and C). Unlike normal myogenesis—where MYOD1 expression emerges in early myoblasts and initiates lineage commitment—MYOD1 activity in *MYOD1*^{L122R}-mutant SRMS was relatively enriched in the progenitor and transition compartments, implicating the L122R mutation in functional uncoupling of MYOD1 from its normal differentiation program (Fig. 3F and figs. S2C and S3A). The transition state exhibited intermediate differentiation potential, partial activation of myogenic regulators such as myosin VI (MYO6), and the highest proportion of proliferative cells, suggesting a tumor-expanding compartment that has yet to enter terminal differentiation (Fig. 3, D to F, and fig. S2, A to C). Cells that do enter terminal differentiation comprise the differentiated state, composed of cells with low CytoTRACE scores, activation of a myocyte gene signature, and increased activity of late-stage myogenic effectors including MYOG, caldesmon 1 (CALD1), myosin IXA (MYO9A), and actinin alpha 2 (ACTN2) (Fig. 3, D, F, and G, and fig. S2, B and C). However, the limited activity of critical regulators such as MYOD1 and myoferlin (MYOF) in this state suggests that these tumors progress to only a partially differentiated end point, lacking a fully functional terminal differentiation program (Fig. 3F and fig. S2C).

Comparative regulatory network analysis of FP/FN-RMS reveals shared and unique *MYOD1*^{L122R}-associated regulatory programs

To contextualize these findings, we next compared the three *MYOD1*^{L122R}-mutant SRMS-derived cell states with the transcriptional programs of FP- and FN-RMS from a recently published integrated single-cell atlas (*13*). To ensure methodological consistency, we reanalyzed six FP-RMS and six FN-RMS *MYOD1*^{WT} samples from this atlas using the same ARACNe/VIPER regulatory network pipeline applied to the *MYOD1*^{L122R}-mutant SRMS samples. We first reconstructed de novo sample-specific tumor regulatory networks

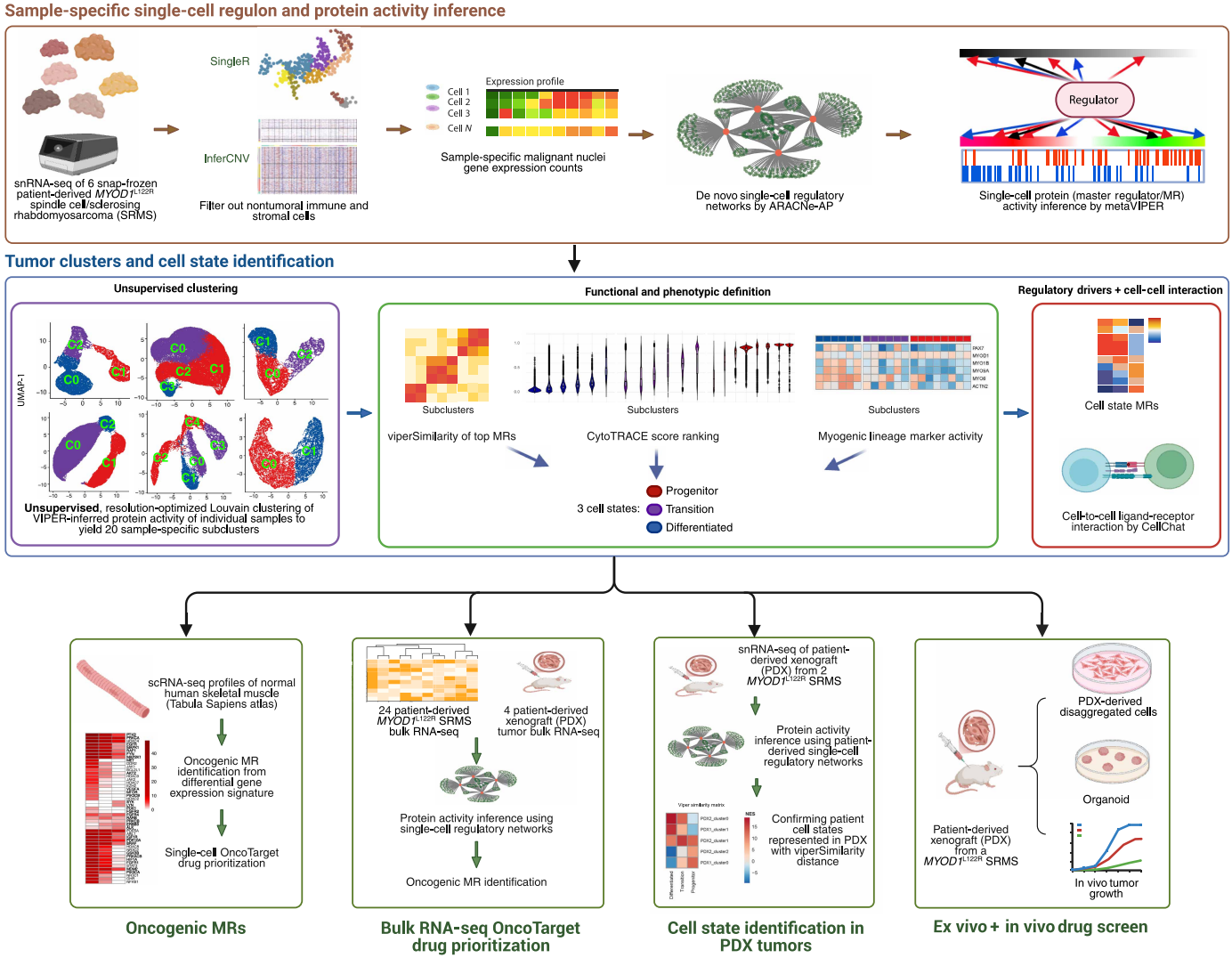

Fig. 2. Visual description of the complete workflow in this study. Schematic outlining the full pipeline used in the analysis of the six snRNA-seq profiles, including regulatory network inference by ARACNe and VIPER, unsupervised clustering and functional/phenotypic cell state determination, identification of oncogenic master regulators, and functional validation of their targeting in in vitro and in vivo models. Specifically, regarding cell state determination, sample-specific tumor clusters were first identified through unsupervised, resolution-optimized Louvain clustering on VIPER-inferred protein activity [(*22*) and detailed in Materials and Methods], yielding 20 subclusters across the six tumors. Three consensus cell states were then defined by statistically significant overlap of the subcluster protein activity profiles (assessed by viperSimilarity, which computes a normalized enrichment score (NES) reflecting the overlap of top and bottom VIPER-inferred master regulators between two signatures) and by concordant patterns of myogenic lineage marker activity and CytoTRACE differentiation scores.

with ARACNe-AP and inferred protein activity from internally scaled differential gene expression signatures using VIPER. We then generated integrated cell state–specific protein activity signatures for the previously annotated FP/FN-RMS progenitor, proliferative, and differentiated cell states and assessed shared enrichment of cell state MR protein activity compared with the *MYOD1*^{L122R}-mutant SRMS states by viperSimilarity (fig. S3B).

This analysis revealed that the *MYOD1*^{L122R}-mutant SRMS differentiated state shares statistically significant overlap in MR proteins with the differentiated FP/FN-RMS cell states, while the *MYOD1*^{L122R}-mutant SRMS transition state is significantly enriched in regulators characteristic of the FP/FN-RMS proliferative and progenitor states, consistent with its less differentiated phenotype and higher proliferative fraction. In contrast, the *MYOD1*^{L122R}-mutant SRMS progenitor state exhibited statistically significant overlap only with the FN-RMS proliferative state, likely reflecting its relatively elevated proliferative fraction. These findings indicate that *MYOD1*^{L122R}-mutant SRMS aligns along a similar myogenic differentiation trajectory observed across RMS subtypes yet also harbors a uniquely rewired progenitor-like compartment with a transcriptionally distinct regulatory program.

To further validate the reproducibility of these cell states and address potential differences in cell state nomenclature across studies, we analyzed an external snRNA-seq dataset containing a single tumor of a patient with *MYOD1*^{L122R}-mutant SRMS [sample 29806 (*15*)]. Unsupervised clustering of metaVIPER-inferred protein activity in this sample recapitulated the same three cell states defined in our primary dataset (fig. S4A). We found statistically significant overlap of MR protein activities between the sample's unsupervised clusters

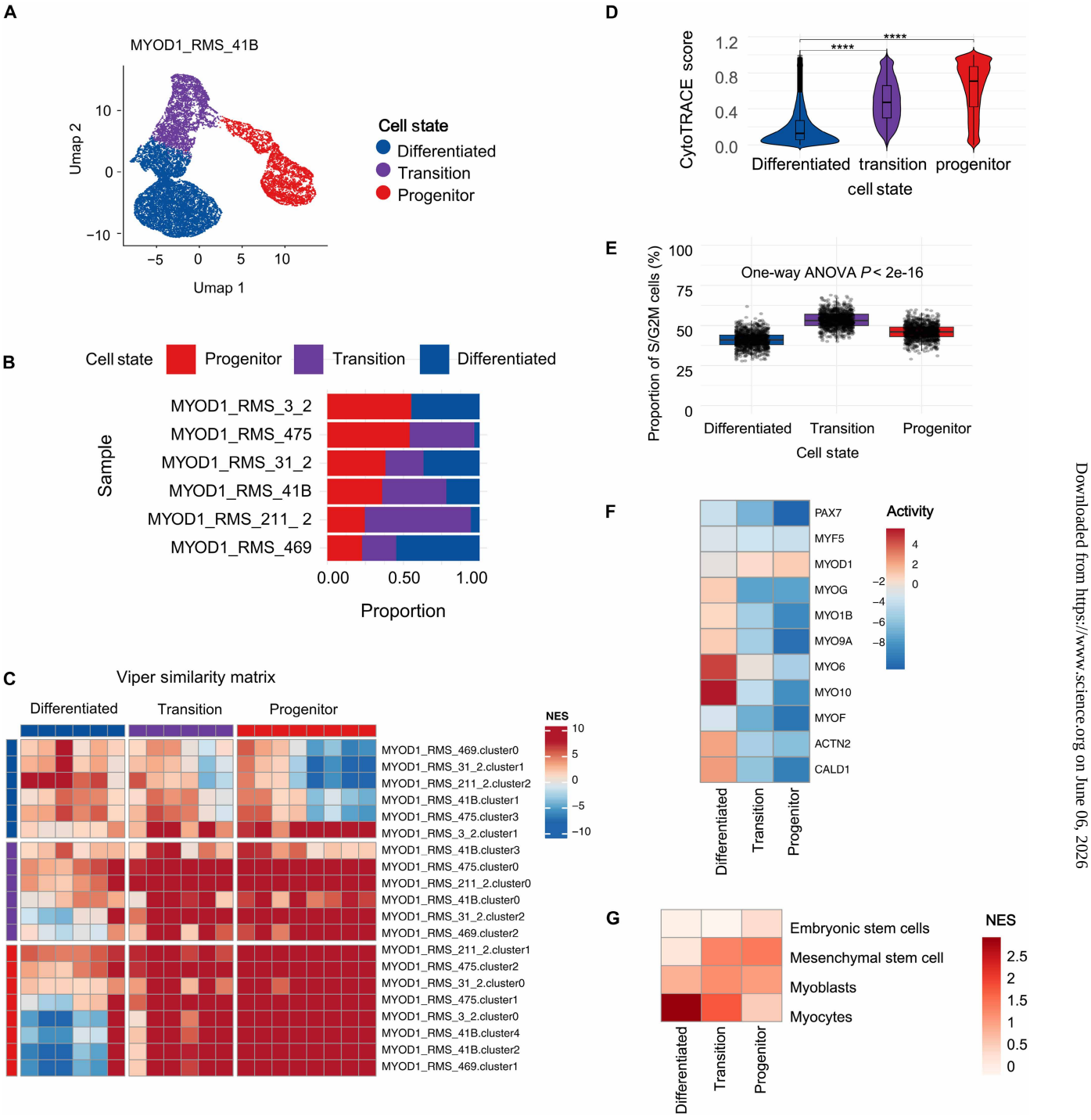

Fig. 3. Single-cell protein activity analysis and cell state determination in *MYOD1*^{L122R}-mutant SRMS. (**A**) UMAP embedding of malignant nuclei from a representative sample (RMS.469), based on VIPER-inferred protein activity, annotated by cell state. (**B**) Distribution of cell state proportions (*x* axis) across six patient-derived tumors (*y* axis), demonstrating that cell states coexist across samples. (**C**) Heatmap of viperSimilarity normalized enrichment scores (NES) quantifying pairwise similarity between subcluster mean protein activity signatures, relative to common reference, as assessed by analytic rank-based enrichment analysis (aREA) of subcluster MRs. Similarity is shown on a color scale of red (high similarity) to blue (inverse enrichment). Subclusters were derived from sample-specific VIPER-inferred protein activity profiles clustered by resolution-optimized Louvain clustering and grouped by similarity into three recurrent tumor cell states: progenitor, transition, and differentiated. (**D**) Violin plots of CytoTRACE scores by cell state. CytoTRACE estimates differentiation potential, with higher values indicating less differentiated (more progenitor-like) states. Pairwise comparisons were performed using two-sided *t* tests after Bonferroni correction; ****$P < 0.0001$. (**E**) Distribution of S and G2M–phase proliferative cell fractions (Seurat cell cycle scoring) across 1000 random subsamples of 100 cells per cell state. One-way analysis of variance (ANOVA) revealed significant differences across states. (**F**) Heatmap of Stouffer-integrated VIPER-inferred protein activity for canonical myogenic regulators across the three cell states. (**G**) Heatmap of enrichment scores, computed by aREA, for gene sets representing lineages along myogenic differentiation [scType (*49*)] in the Stouffer-integrated protein activity signature of each cell state.

and the *MYOD1*^{L122R}-mutant SRMS cell states as assessed by viper-Similarity, including for those most significantly driving differentiation cell fate by CytoTRACE correlation (fig. S4, B and C). This sample was primarily composed of *MYOD1*^{L122R}-mutant SRMS transition and differentiated cells, and given the prior analysis showing that the FP/FN-RMS progenitor state corresponds most closely to the *MYOD1*^{L122R}-mutant SRMS transition state, our analysis biologically aligns with the prior finding in (*13*) that this sample expresses primarily the FP/FN-RMS progenitor signature.

Next, given the central role of MYOD1 in myogenic differentiation, we examined whether the differences in cell state organization were associated with altered MYOD1 activity or regulatory rewiring. Comparative analysis of VIPER-inferred MYOD1 activity across the defined cell states in the FP/FN-RMS and *MYOD1*^{L122R}-mutant SRMS datasets revealed opposing trajectories: In *MYOD1*^{L122R}-mutant SRMS, MYOD1 activity was relatively enriched in progenitor-like cells and decreased with differentiation, whereas in FP/FN-RMS, MYOD1 activity is higher in differentiated states (fig. S3A). While modest in magnitude, this inversion suggests that the *MYOD1*^{L122R} mutation alters its normal regulatory trajectory, sustaining a distinct progenitor-like program and shifting the differentiation landscape.

To determine whether these changes reflected an intrinsic rewiring of MYOD1 regulatory networks, we compared the regulons inferred de novo from *MYOD1*^{L122R}-mutant SRMS and FP/FN-RMS datasets. The MYOD1^{L122R} regulon, comprising 134 statistically significant direct targets, and the MYOD^{WT} regulon, comprising 209 significant direct targets, exhibited minimal overlap (11 shared genes), indicating that mutant and wild-type MYOD1 control largely distinct transcriptional programs (fig. S3C). Both regulons were enriched for known MYOD1 binding sites by ENCODE chromatin immunoprecipitation sequencing (*35*), confirming that ARACNe captured bona fide MYOD1-related interactions but activated divergent biological functions. The MYOD1^{WT} regulon was enriched for canonical myogenic (e.g., ACTC1, CDH15, TPM2, ENO3, and DMPK) and RNA-processing (e.g., HNRNP and SRSF proteins) genes, whereas the MYOD^{L122R} regulon included targets associated with PI3K/AKT/mTOR signaling and MYC-like biosynthetic pathways (e.g., DICER1, CELF1, MBNL1, TRA2A, SON, SUPT16H, CHD3).

Functional enrichment of these target sets using Enrichr (MSigDB hallmark 2020 gene sets) further underscored this divergence (*36*–*38*). The MYOD1^{WT} regulon showed significant enrichment for "Myogenesis" (adjusted $P = 0.005$) and "Apical Junction," together with "Myc Targets V1," reflecting activation of muscle-lineage and cytoskeletal programs. In contrast, the MYOD1^{L122R} regulon lacked enrichment for myogenic pathways and instead exhibited statistically significant enrichment for "Mitotic Spindle" (adjusted $P = 0.002$), along with "UV Response Up", "Myc Targets V1," and "Protein Secretion"—hallmarks of proliferative and anabolic transcriptional states. Together, these findings support that MYOD1^{L122R} rewires its regulatory network away from canonical myogenic differentiation toward proliferative, biosynthetic, and MYC-like programs, driving loss of lineage fidelity and potentially contributing to the persistence of a unique, progenitor-biased transcriptional state in *MYOD1*^{L122R}-mutant SRMS.

Paracrine IGF2–IGF1R signaling and MYOD1 dysregulation sustain the aberrant differentiation hierarchy in *MYOD1*^{L122R}-mutant SRMS

To identify candidate regulators of the *MYOD1*^{L122R}-mutant SRMS cell state architecture, we next evaluated cell state–specific metaVIPER-inferred MRs (Figs. 2 and 4A), focusing on those correlated with CytoTRACE-inferred differentiation potential. IGF2 emerged as one of the most activated MRs in the progenitor cell state, significantly associated with high CytoTRACE scores, suggesting a potential role in maintaining a less differentiated phenotype. IGF2 is a fetal growth factor known to support stemness and self-renewal in mesenchymal, embryonic, and neural stem cells (*39*–*41*). In myogenic differentiation, IGF2 promotes MYOD1 induction and myogenic commitment via IGF1R–mediated PI3K/AKT and mitogen-activated protein kinase (MAPK) signaling, as well as recruitment of MYOD1-associated transcriptional machinery at target promoters (*41*–*44*).

In our *MYOD1*^{L122R}-mutant SRMS dataset, progenitor cells displayed high *IGF2* expression and protein activity, along with enriched MYOD1 activity, but lacked expression of *IGF1R* and *IGF2R* (Fig. 3F, Fig. 4A-B), suggesting they may be resistant to autocrine IGF2 signaling. In contrast, transition and differentiated states expressed IGF1R and IGF2R, but had reduced MYOD1 activity (Fig. 3F, Fig. 4A-B). These findings are consistent with a model in which IGF2 signaling, rather than promoting myogenic differentiation via MYOD1, instead functions through a paracrine IGF2–IGF1R signaling axis from progenitor to more differentiated states.

Systematic ligand-receptor analysis using CellChat (*45*) supported this model, identifying progenitor cells as IGF2 "senders" and IGF1R/IGF2R–expressing transition and differentiated cells as "receivers" (Fig. 4C). IGF1 was not detected in any cell state, implicating IGF2 as the primary IGF1R ligand. IGF2R, a nonsignaling decoy receptor (*46*), was most abundant in transition and differentiated cells, potentially buffering IGF2 availability and modulating signal strength. This paracrine IGF2–IGF1R axis may enable progenitor cells to facilitate expansion of downstream states that lack functional MYOD1 activity and are unable to complete the myogenic program.

Consistent with a stemlike identity, progenitor cells were further characterized by MRs involved in proliferation, metabolic reprogramming [e.g., GAPDH, a regulator of metabolic plasticity in cancer stemlike cells], and immune evasion (e.g., MERTK, SYK, FCGR2A, MSR1, LYN, known regulators of macrophage, and innate immune pathways). In contrast, differentiated states exhibited MRs correlated with low CytoTRACE scores and associated with terminal myogenic differentiation and cytoskeletal organization, including PRKG1 and ANKRD1 (Fig. 4A).

IGF2–driven PI3K/AKT/mTOR activation and other oncogenic master regulators as targetable dependencies in *MYOD1*^{L122R}-mutant SRMS

Given the identification of IGF2 and IGF1R as MRs of the progenitor and transition/differentiated cell states, respectively, we next assessed whether this paracrine signaling axis activates downstream PI3K/AKT/mTOR pathway components that may represent conserved, cell state–specific therapeutic vulnerabilities. To identify such oncogenic MRs driving the normal to tumor cell state transition, we inferred protein activity by metaVIPER from the differential expression of *MYOD1*^{L122R}-mutant SRMS tumors relative to normal skeletal muscle (Tabula Sapiens) (table S5) (*47*). We then focused on 182 proteins with known Food and Drug Administration (FDA)–approved or late-stage experimental inhibitors, prioritized based on the OncoTarget precision oncology platform (Fig. 2) (*20*).

Whereas cell state MRs captured regulators unique to distinct tumor subpopulations, the tumor-normal comparison revealed commonly activated oncogenic MRs across all states, alongside a subset

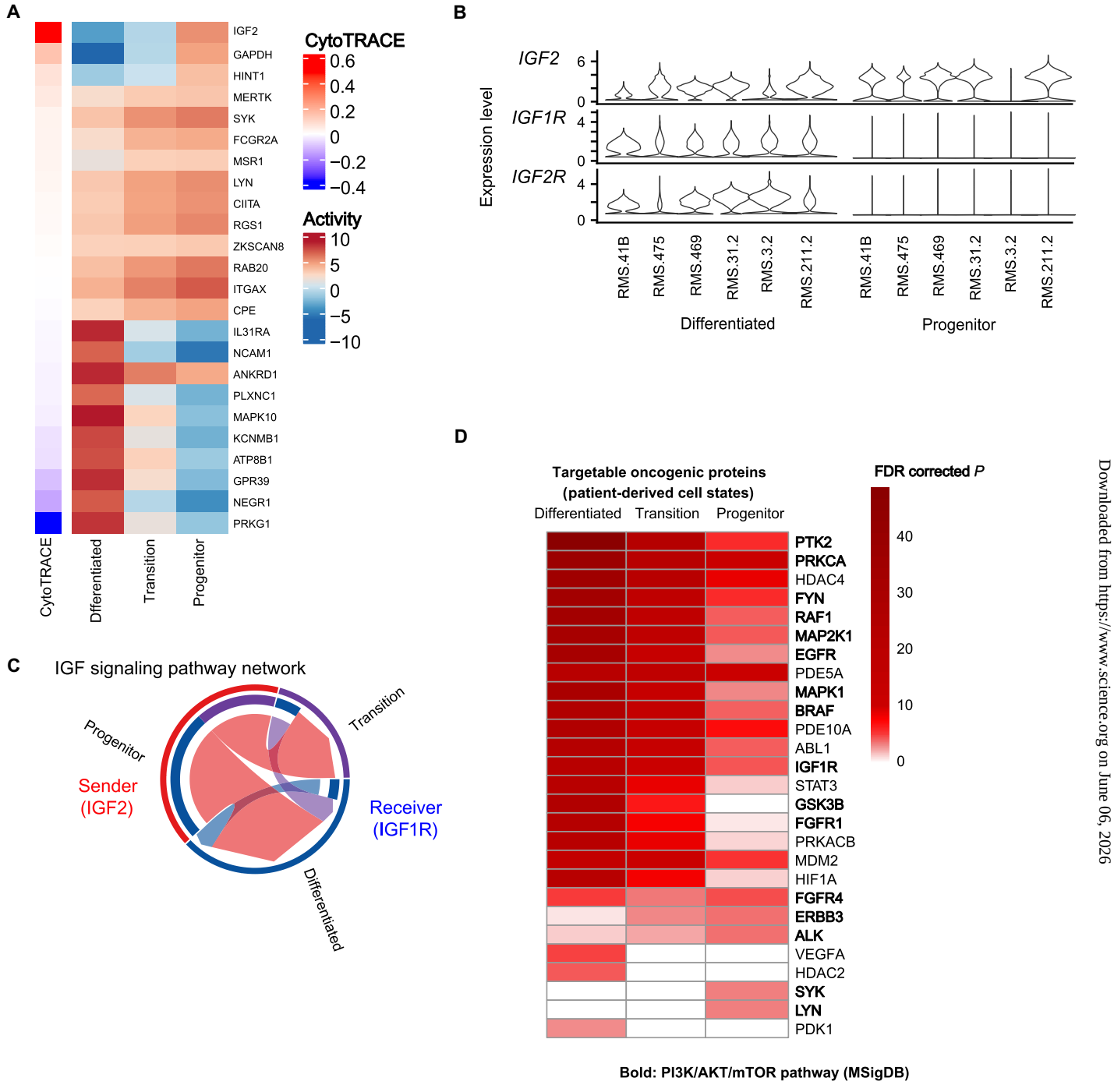

Fig. 4. Single-cell protein activity analysis reveals actionable cell state–specific MRs and a paracrine IGF2–IGF1R–PI3K/AKT/mTOR signaling axis in *MYOD1*^{L122R}-mutant SRMS. (**A**) Heatmap of VIPER-inferred protein activity (right) for the top 15 MRs (rows) most aberrantly activated in the mean protein activity signature of each cell state (columns), ranked by Pearson correlation with CytoTRACE score across all cells. The left heatmap displays the corresponding correlations (red = positive; blue = negative). NES values indicate MR activity (red = activated; blue = inactivated). (**B**) Violin plots of gene expression (RNA assay log normalized counts) for *IGF2*, *IGF1R*, and *IGF2R* across six samples, separated by differentiated (left) and progenitor (right) cell states. *IGF2* is elevated in progenitor cells, which lack *IGF1R* and *IGF2R* expression, while differentiated cells express the receptors. Transition cells showed similar profiles to differentiated cells and were omitted for space. (**C**) Circle plot of inferred IGF signaling interactions generated by CellChat, a computational framework that predicts cell-cell communication from ligand-receptor expression. Progenitor cells are the predominant source of IGF2 ligand (sender), while transition and differentiated cells are primary targets via IGF1R (receiver). (**D**) Heatmap representing the statistical significance [−$\log_{10}$ false discovery rate (FDR)–adjusted *P* values] of OncoTarget-predicted high-affinity drug targets (rows) across patient-derived tumor cell states (columns), based on Stouffer-integrated synthetic bulk VIPER-inferred oncogenic protein activity profiles relative to normal skeletal muscle. Targets are ranked by their mean significance across cell states, highlighting both shared and state-specific oncogenic dependencies in *MYOD1*^{L122R}-mutant SRMS.

of cell state–specific targetable vulnerabilities (Fig. 4D). Among the top-ranking, significantly activated oncogenic MRs (Bonferroni-adjusted $P \leq 10^{-5}$), we observed consistent enrichment for IGF1R/PI3K/AKT/mTOR pathway components (e.g., IGF1R, PIK3CA, and GSK3B), particularly in transition and differentiated states—populations that express IGF1R and receive IGF2–derived paracrine signals (Fig. 4D). While select pathway members were also active in the progenitor state, suggesting broader relevance to tumor maintenance across the differentiation spectrum, the progenitor state also displayed uniquely activated, targetable oncogenic MRs including protein tyrosine kinase 2 (PTK2), SYK, LYN, and ALK—proteins implicated in immune signaling, stemness, and tumor progression—highlighting potential orthogonal, state-specific therapeutic strategies for combination approaches.

PDX models recapitulate *MYOD1*^{L122}-mutant SRMS intratumor heterogeneity and regulatory architecture

To assess whether *MYOD1*^{L122R}-mutant SRMS PDX models faithfully preserve the transcriptional and regulatory heterogeneity observed in patient tumors, we analyzed snRNA-seq profiles from two PDX models: MSKRMS-93202.T1 (derived from patient RMS211.2 in our cohort) and MSKRMS-74711 [previously published (*15*)]. We inferred tumor single-nucleus protein activity with metaVIPER using the previously generated patient-derived gene regulatory networks, generating protein activity signatures across 10,677 tumor nuclei from the two PDX models (Fig. 2).

Unsupervised clustering of metaVIPER-inferred protein activity (resolution-optimized Louvain algorithm; see Materials and Methods) identified two tumor cell clusters in MSKRMS-74711 and three in MSKRMS-93202 (Fig. 5A). These showed strong concordance with the progenitor and more differentiated cell states observed in patient tumors (Fig. 5B). Specifically, the top and bottom 50 MRs in each PDX cluster statistically significantly overlapped with the MR profiles of the patient-derived progenitor or transition/differentiated states, including high activity of IGF2 and MYOD1 in the progenitor-like clusters, and PRKG1, CALD1, MYOG in the more differentiated-like clusters (Fig. 5, B to D).

Notably, in the RMS211.2 patient tumor, ~25% of cells were classified as progenitor, with the remainder annotated as transition and differentiated, and we observed a similar segregation of progenitor and more differentiated cells in the corresponding PDX model, in which the transition and differentiated states showed significant overlap and were considered as one more differentiated-like state. Collectively, these findings demonstrate that *MYOD1*^{L122R}-mutant SRMS PDX models retain the cell state architecture and regulatory programs of their tumors of origin, supporting their use as tractable preclinical models for functional validation and therapeutic testing.

To determine whether the candidate therapeutic vulnerabilities were conserved in PDX models, we inferred oncogenic protein activity by metaVIPER relative to normal skeletal muscle from bulk RNA-seq generated on *MYOD1*^{L122R}-mutant SRMS PDX tumors (MSKRMS-74711 and MSKRMS-93202, including three multifocal recurrent metastatic samples: T1, T2, and T3) (table S6). The oncogenic MRs across all four PDX tumors were enriched for PI3K/AKT/mTOR pathway targets, consistent with those identified from single-cell analyses, further supporting the use of these models for functional validation (Fig. 5E).

Bulk transcriptomics recapitulates actionable MRs of *MYOD1*^{L122R}-mutant SRMS cell states

We further validated cell state MR signatures identified by single-cell analysis in a larger cohort of 24 *MYOD1*^{L122R}-mutant SRMS bulk RNA-seq samples (Fig. 2). Unsupervised clustering of metaVIPER-inferred protein activity profiles derived from internally scaled bulk gene expression signatures (table S7) stratified the 24 samples into three transcriptionally distinct groups, whose average MR activity profiles broadly overlapped with the progenitor and differentiated single-cell state MRs (Fig. 6, A to C). Bulk cluster 2, whose sample MRs were most significantly enriched in the transition/differentiated cell state protein activity signatures, recapitulated the more differentiated program, while bulk cluster 3, whose sample MRs were most significantly enriched in the progenitor cell state protein activity signature, recapitulated the progenitor program (Fig. 6, B and C). Notably, bulk cluster 1 lacked clear enrichment for any single-cell state, potentially reflecting limitations of bulk analyses due to either averaging of signals across more equally coexisting transcriptionally distinct states or influence of nonmalignant components. Therefore, while bulk data validated MRs of predominant cell states in tumor samples in an expanded cohort, bulk profiling alone remains limited in resolving tumor-intrinsic heterogeneity.

We then assessed oncogenic MR activity in the *MYOD1*^{L122R}-mutant SRMS bulk cohort by inferring sample-specific protein activity from differential gene expression signatures computed relative to normal skeletal muscle, prioritizing actionable MRs by OncoTarget as previously described. This confirmed that the most significantly activated oncogenic MRs (Bonferroni-adjusted $P \leq 10^{-5}$) were highly conserved across samples and enriched in targets involved in the IGF1R-PI3K/AKT/mTOR pathway, similar to those identified from the single-cell analysis, although missing their cell state specificity (Fig. 6D).

Genomic profiling of *MYOD1*^{L122R}-mutant SRMS reveals recurrent IGF2–PI3K/AKT/mTOR pathway alterations in subsets of patients

To understand the potential intersection of genomic alterations with the transcriptional programs identified in patients with *MYOD1*^{L122R}-mutant SRMS, we evaluated genomic profiles from 20 unique patients with *MYOD1*^{L122R}-mutant SRMS profiled by MSK-IMPACT [a targeted 341–505 gene matched tumor-normal DNA sequencing panel (*33*)]. These samples reflect the poor outcomes seen in this disease with median disease-specific survival (DFS) and progression-free survival (PFS) of 42.4 and 27.3 months, respectively, and 5-year disease-specific survival (DSS) and PFS of 35 and 29%, respectively (Fig. 7, A and B).

The VAF of *MYOD1* was greater than 50% in all except one case (range: 0.43 to 0.98, median: 0.78). This is consistent with either homozygosity of the *MYOD1*^{L122R} mutation or relative enrichment of mutant alleles due to chromosome 11p aneuploidy, which was observed in a subset of tumors, including five with high-level 11p amplification (Fig. 7, C and D). The most highly recurrent co-occurring pathogenic or likely pathogenic genomic variants were *IGF2* amplification and alterations involving genes in the PI3K/AKT/mTOR pathway (*PIK3CA*: 20%, *PTEN*: 10%; *AKT*, *PIK3R3*, and *PIK3C2G*: 5% each) (Fig. 7C). These co-occurring genomic alterations were notably almost entirely mutually exclusive and enriched in posttreatment samples (Fig. 7C). Other recurrent genomic alterations (5 to 15%) include variants affecting genes upstream of PI3K/AKT/mTOR (*NF1*, *NF2*, *NRAS*, *BCOR*, and *FGFR4*), *MDM2*/*CDK4* amplification, and

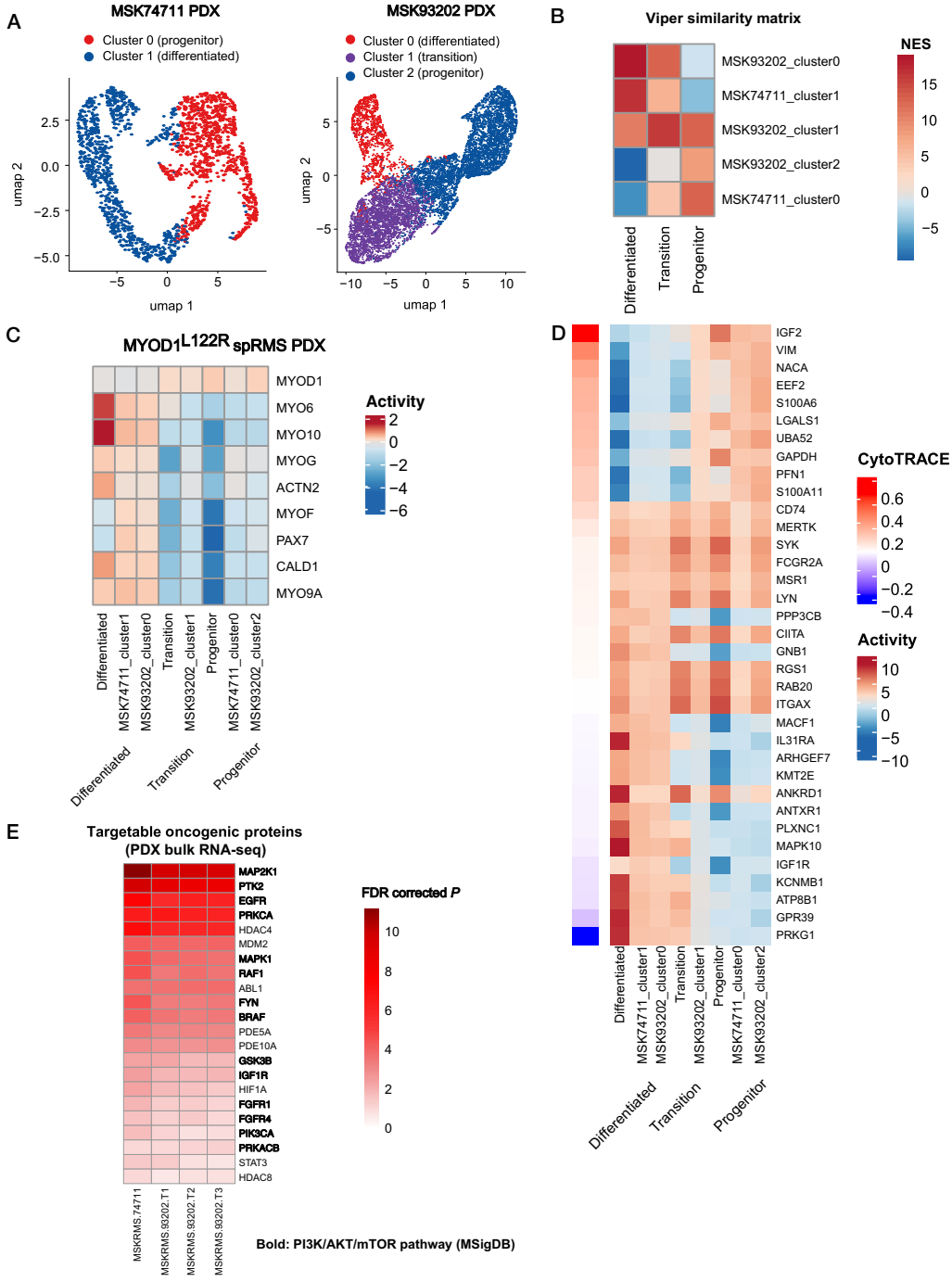

Fig. 5. PDX models recapitulate *MYOD1*^{L122}-mutant SRMS intratumor heterogeneity, regulatory architecture, and targetable oncogenic master regulators. (**A**) UMAP embeddings of malignant nuclei from two *MYOD1*^{L122R}-mutant PDX models (MSKRMS-74711 and MSKRMS-93202.T1), based on VIPER-inferred protein activity. Cells are colored by resolution-optimized Louvain clusters. (**B**) Heatmap of viperSimilarity NES quantifying pairwise similarity between PDX subcluster mean protein activity signatures and those of the three patient tumor cell states (differentiated, transition, and progenitor), based on overlap of the top 100 aberrantly activated MRs. NES values are displayed on a color scale from red (high similarity) to blue (inverse enrichment). On the basis of these similarity scores, each PDX cluster could be confidently assigned to a corresponding patient-derived cell state. (**C**) Heatmap of mean VIPER-inferred protein activity scores for canonical myogenic regulators across each PDX subcluster and patient-derived state, grouped by cell state identity, showing similar patterns across patient and PDX cell states. (**D**) Heatmap of VIPER-inferred protein activity for the top 15 most aberrantly activated MRs (rows) in each PDX- and patient-derived state (columns), grouped by cell state identity. MRs are ranked by their Pearson correlation with CytoTRACE score, with the corresponding correlation values shown in the adjacent heatmap (left). Key differentiation-enforcing cell state–specific MRs are conserved across patient and PDX tumors. (**E**) Heatmap showing statistical significance (−$\log_{10}$ FDR-adjusted *P* values) of OncoTarget-predicted high-affinity drug targets (rows) across four *MYOD1*^{L122R}-mutant SRMS PDX models profiled by bulk RNA-seq (columns), based on VIPER-inferred oncogenic protein activity relative to normal skeletal muscle. Patient-derived cell state dependencies were recapitulated in PDX models. Genes belonging to the IGF1R-PI3K/AKT/mTOR signaling pathway (MSigDB hallmark) are highlighted in bold.

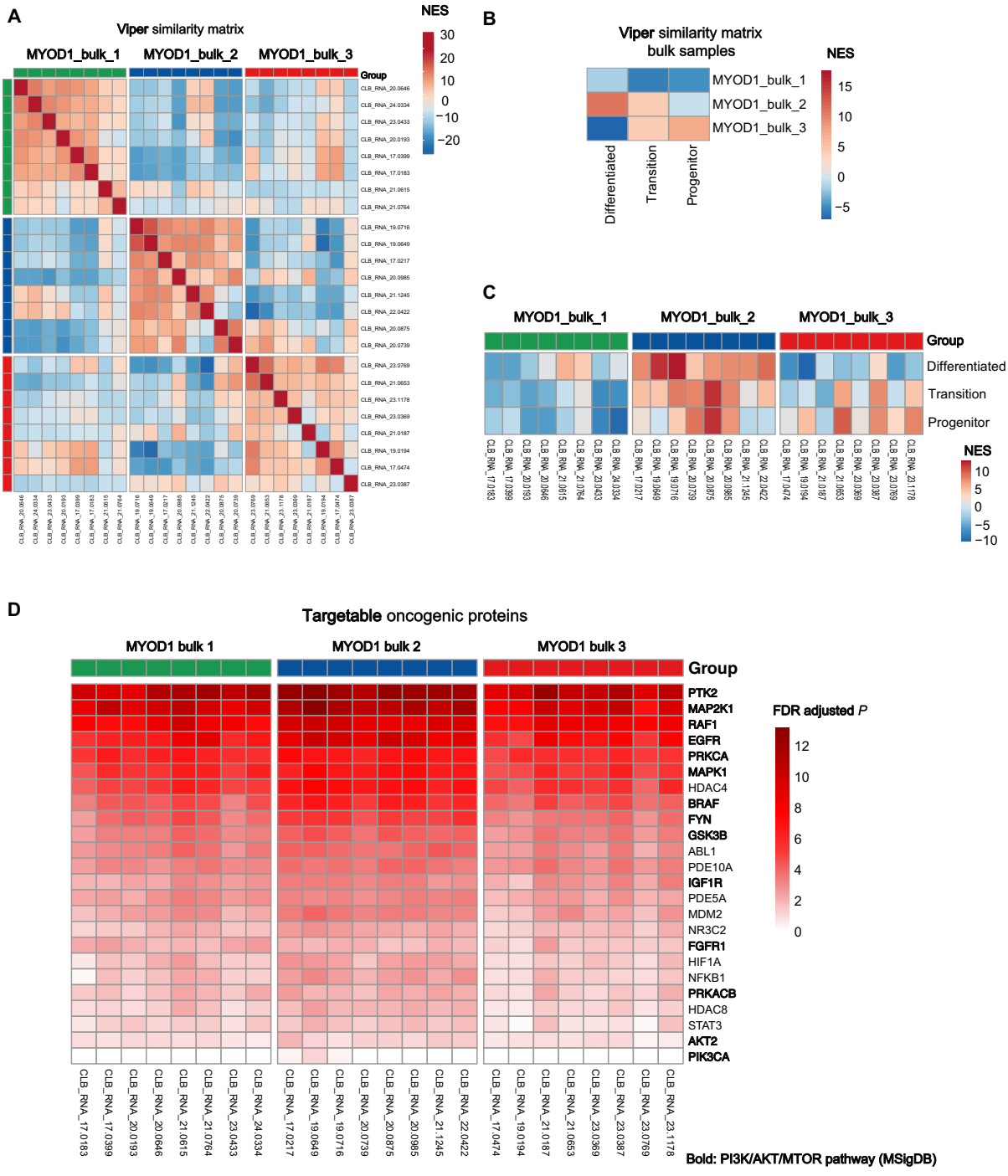

Fig. 6. Bulk transcriptomics recapitulates actionable MRs of *MYOD1*^{L122R}-mutant SRMS cell states. (**A**) Heatmap of viperSimilarity NES quantifying pairwise similarity between VIPER-inferred protein activity signatures of 24 *MYOD1*^{L122R}-mutant SRMS bulk RNA-seq samples. NES values reflect the enrichment of the top 100 aberrantly activated MRs in each pairwise comparison, displayed on a color scale from red (high similarity) to blue (inverse enrichment). Samples were clustered into three groups based on similarity based on optimum average silhouette width using the partition around medoids (PAM) method. (**B**) Heatmap of viperSimilarity NES values comparing the mean protein activity signature of each bulk cluster to the mean protein activity signature of the three patient-derived single-cell tumor cell states, demonstrating stratification of bulk samples into progenitor-like (bulk cluster 3) and differentiated-like (bulk cluster 2) groups, as well as a group (bulk cluster 1) that did not show significant overlap with any individual single-cell state. (**C**) Heatmap of NES computed by aREA reflecting the enrichment of the top 100 cell state–specific MRs for each single-cell state in each bulk sample protein activity signature, demonstrating significant enrichment of differentiated cell state MRs in samples belonging to bulk cluster 2 and progenitor cell state MRs in samples belonging to bulk cluster 3. (**D**) Heatmap showing statistical significance ($-\log_{10}$ FDR-adjusted *P* values) of OncoTarget-predicted high-affinity drug targets (rows) across the 24 *MYOD1*^{L122R}-mutant SRMS bulk samples (columns), based on VIPER-inferred oncogenic protein activity relative to normal skeletal muscle. This larger bulk cohort recapitulated shared oncogenic dependencies identified by single-cell analysis, including enrichment of targets belonging to the IGF1R-PI3K/AKT/mTOR signaling pathway (MSigDB hallmark), which are highlighted in bold.

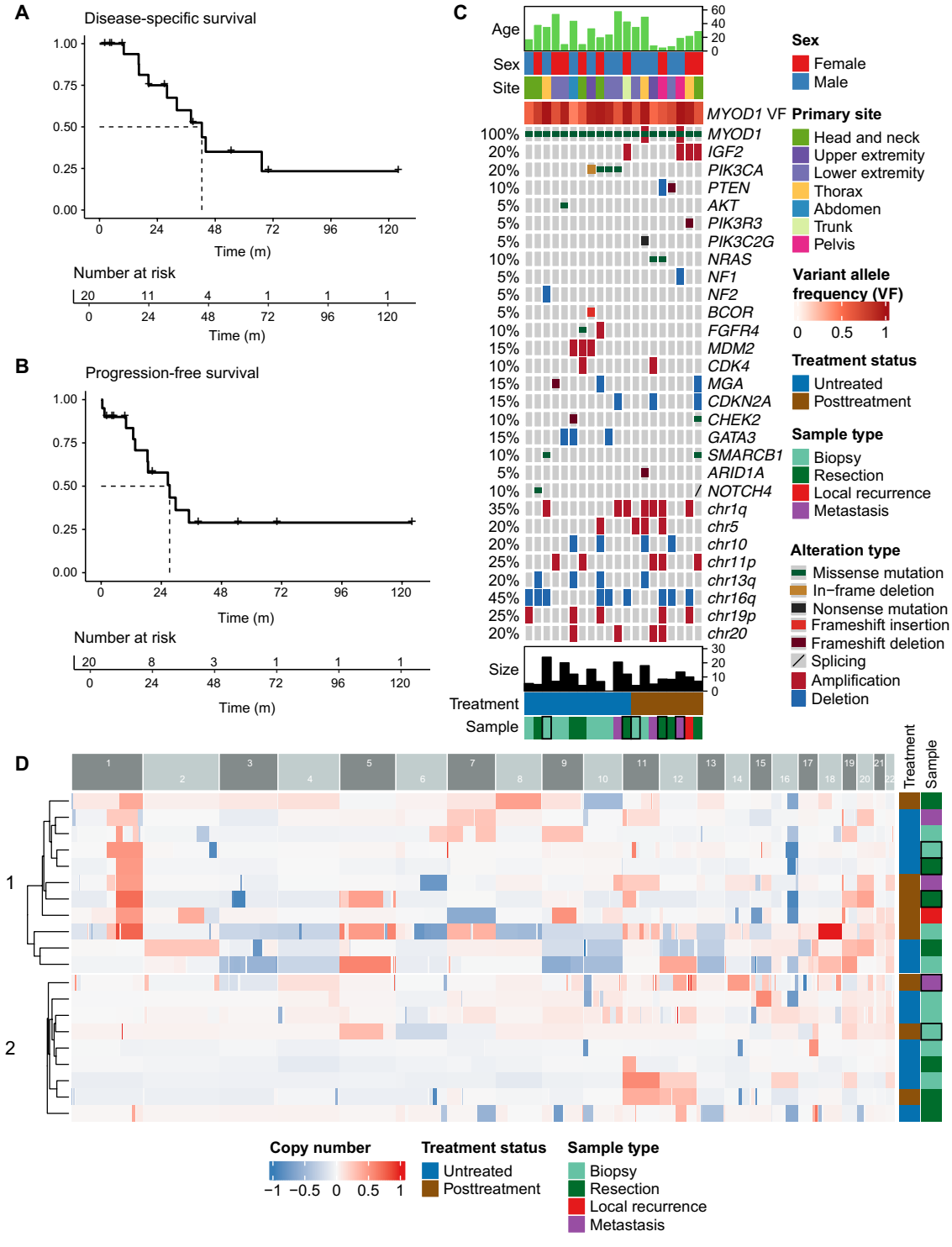

Fig. 7. Genomic profiling of *MYOD1*^{L122R}-mutant SRMS reveals recurrent IGF2–PI3K/AKT/mTOR pathway alterations and copy number heterogeneity across clinical samples. (**A** and **B**) Kaplan-Meier curves depicting disease-specific survival (DFS) (A) and progression-free survival (PFS) (B) in a cohort of 20 patients with *MYOD1*^{L122R}-mutant SRMS. Survival analyses are based on time from diagnosis, with tick marks indicating censoring and number at risk provided for each time point below each plot. (**C**) Oncoprint summarizing the frequency and distribution of somatic alterations identified by MSK-IMPACT–targeted sequencing across the 20 patient tumors, which are further annotated by corresponding clinical features [age, sex, primary tumor site, treatment status, sample type, and *MYOD1* variant allele frequency (VAF)]. Individual patients included in this study are denoted by black outline. (**D**) Unsupervised hierarchical clustering of arm-level chromosomal copy number profiles across the tumors. Values represent relative copy number changes, annotated by treatment status and sample type. Two major copy number alteration (CNA)-defined clusters emerged, each encompassing tumors across diverse clinical settings. Individual patients included in this study are denoted by black outline. m, months.

inactivating mutations or copy number deletions in *MGA*, *CDKN2A*, *CHEK2*, *SMARCB1*, *ARID1A*, and *NOTCH4*. In addition, recurrent (20 to 45%) chromosomal arm-level changes include amplifications in chr1q, 5, 11p, 19p and 20 and deletions in chr10, 13q, and 16q (Fig. 7, C and D).

Four of the six patients with *MYOD1*^{L122R}-mutant SRMS and the two PDX models (MSK-93202 and MSK-74711) profiled by snRNA-seq were among the 20 patients who underwent genomic profiling: RMS3.2 (*IGF2* amplification and *NF1* deletion), RMS211.2 (MSK-93202) (*NRAS* mutation, *PTEN* deletion, chr1q, 5, 11p, 19p, 20 amplification, and chr16q deletion), RMS469 (*NF2* deletion, *SMARCB1* mutation, chr1q amplification, and chr16q deletion), RMS475 (chr5 amplification), and MSK-74711 (*IGF2* amplification) (Fig. 7C and table S2). These genomic findings reinforce the central role of IGF2–IGF1R–PI3K/AKT/mTOR signaling in *MYOD1*^{L122R}-mutant SRMS, with regulatory network analysis of single-cell profiles suggesting the convergence of these heterogeneous co-occurring genomic alterations on shared transcriptional programs that coexist across all patients, independent of mutational status.

Functional validation of IGF2–IGF1R–PI3K/AKT/mTOR signaling as a therapeutic dependency in *MYOD1*^{L122R}-mutant SRMS

Having identified activation of the IGF2–IGF1R–PI3K/AKT/mTOR axis through regulatory network analysis of single-cell profiles, reinforced by analysis of bulk transcriptomic and genomic data, across a large molecularly profiled cohort of patients with *MYOD1*^{L122R}-mutant SRMS, we sought to functionally validate this pathway as a therapeutic vulnerability for clinical translation (Fig. 2).

To first functionally validate the presence of an IGF2–IGF1R–PI3K/AKT signaling axis in *MYOD1*^{L122R}-mutant SRMS, we stimulated cell cultures derived from MSKRMS-74711 and MSKRMS-93202.T3 with exogenous IGF2 ligand. This induced ligand-dependent phosphorylation of AKT and extracellular signal–regulated kinase (ERK; Fig. 8A), supporting activation of canonical PI3K and MAPK signaling downstream of IGF2 in *MYOD1*^{L122R}-mutant SRMS.

We next performed ex vivo drug screens using disaggregated tumor cells from both PDX models to evaluate sensitivity to a panel of IGF1R/PI3K/AKT/mTOR–targeting compounds (Table 2 and figs. S5 and S6). A subset of inhibitors demonstrated submicromolar activity, including AZD8055 (mTOR inhibitor), LY3023414 (dual PI3K/mTOR inhibitor), and A-674563 (AKT1 inhibitor), or low micromolar activity, including GSK1838705A (IGF1R inhibitor) (Fig. 8B). In contrast, the *MYOD1*^{L122R}-mutant SRMS cells were resistant to standard chemotherapeutic agents commonly used in the relapse setting, including SN-38 [active metabolite of irinotecan (Irino)] and temozolomide (TMZ) [median inhibitory concentration (IC_{50}) > 29 and > 100 μM, respectively], underscoring their chemotherapy-resistant phenotype.

Given our model that IGF2–driven PI3K/AKT/mTOR signaling sustains the proliferative transition and differentiated tumor cell states and enrichment of pathway alterations in posttreatment samples, we hypothesized that this pathway may contribute to chemotherapy resistance. We thus evaluated whether cotargeting the PI3K/mTOR axis could enhance the efficacy of Irino and/or TMZ by performing combination drug screens pairing one of the most potent PI3K/mTOR inhibitors (LY3023414) with SN-38 and/or TMZ, testing both dual and triple-drug regimens. These combination screens revealed additive and/or synergistic effects in *MYOD1*^{L122R}-mutant SRMS cells, with the greatest synergy observed in MSKRMS-93202.T3 for the combination of LY3023414 with Irino and TMZ (fig. S7). While the response was more modest in MSKRMS-74711, the triple combination consistently produced a positive Bliss synergy score across both models.

To further evaluate therapeutic vulnerabilities in a biologically relevant system that may better preserve the intercellular signaling and differentiation hierarchies of *MYOD1*^{L122R}-mutant SRMS, we assessed drug responses in a patient-derived tumor three-dimensional (3D) organoid (PDXO) generated from the MSKRMS-93202.T1 [Fig. 8C and (*48*)]. Unlike dissociated in vitro cultures, organoids can retain features of 3D organization, maintaining aspects of tumor architecture and cellular communication, potentially better capturing paracrine interactions—such as IGF2–IGF1R signaling—which underlie cell state dynamics and therapeutic response. Consistent with the chemotherapy-resistant phenotype observed in PDX-derived cells, the *MYOD1*^{L122R}-mutant SRMS PDXOs tested in our mini-ring platform demonstrated heightened resistance to a broad spectrum of agents compared to other RMS subtypes and sarcomas [Fig. 8D and (*48*)]. Despite this, the SRMS PDXOs were relatively more sensitive to ceritinib (ALK inhibitor), copanlisib (PI3K inhibitor), linsitinib (IGF1R inhibitor), linsitinib + palbociclib (CDK4/6 inhibitor), and sapanisertib (mTORC1/2 inhibitor) (Fig. 8D, Table 3, and table S8). The greater relative activity in the organoid model to IGF1R inhibition than in dissociated cell screens potentially reflects context-specific IGF1R dependency only evident in models preserving cell-cell signaling.

To dissect pathway-level vulnerabilities, we ranked the viability effects of each compound in the mini-ring screen and visualized the resulting response percentiles after merging agents into their primary mechanistic classes (Fig. 8E). This distribution segregates bona fide vulnerabilities, drug classes whose median percentile lies at or below the predefined 25% sensitivity threshold, from pathways with only moderate or negligible impact. Among classes with multiple agents tested, three satisfied this criterion: PI3K/AKT/mTOR inhibitors, IGF1R inhibitors, and DNA-synthesis blockers, each containing highly effective agents and a class median at or below the threshold. These findings further validated IGF1R and its downstream PI3K/AKT/mTOR pathway as dependencies in *MYOD1*^{L122R}-mutant SRMS.

In vivo efficacy of PI3K/mTOR inhibition and combination therapy in *MYOD1*^{L122R}-mutant SRMS

Building on the ex vivo and organoid findings that *MYOD1*^{L122R}-mutant SRMS depends on IGF2–IGF1R–PI3K/mTOR signaling, we next sought to determine whether pharmacologic inhibition of this pathway could suppress tumor growth in vivo and enhance the efficacy of cytotoxic chemotherapy. To this end, we treated the *MYOD1*^{L122R}-mutant SRMS PDX model (MSKRMS-93202.T3) with the dual PI3K/mTOR inhibitor LY3023414, either as monotherapy or in combination with Irino + TMZ—agents commonly used in relapsed RMS regimens.

Using clinically relevant dosing and schedules ($n = 8$ mice per arm), all treatment groups (LY3023414, Irino + TMZ, and the triple combination) demonstrated significantly improved tumor volume (TV) control at end of treatment compared with the vehicle ($P = 0.0003$ for all comparisons). While Irino + TMZ produced greater tumor suppression than LY3023414 alone ($P = 0.0003$), monotherapy with LY3023414 nonetheless achieved meaningful antitumor

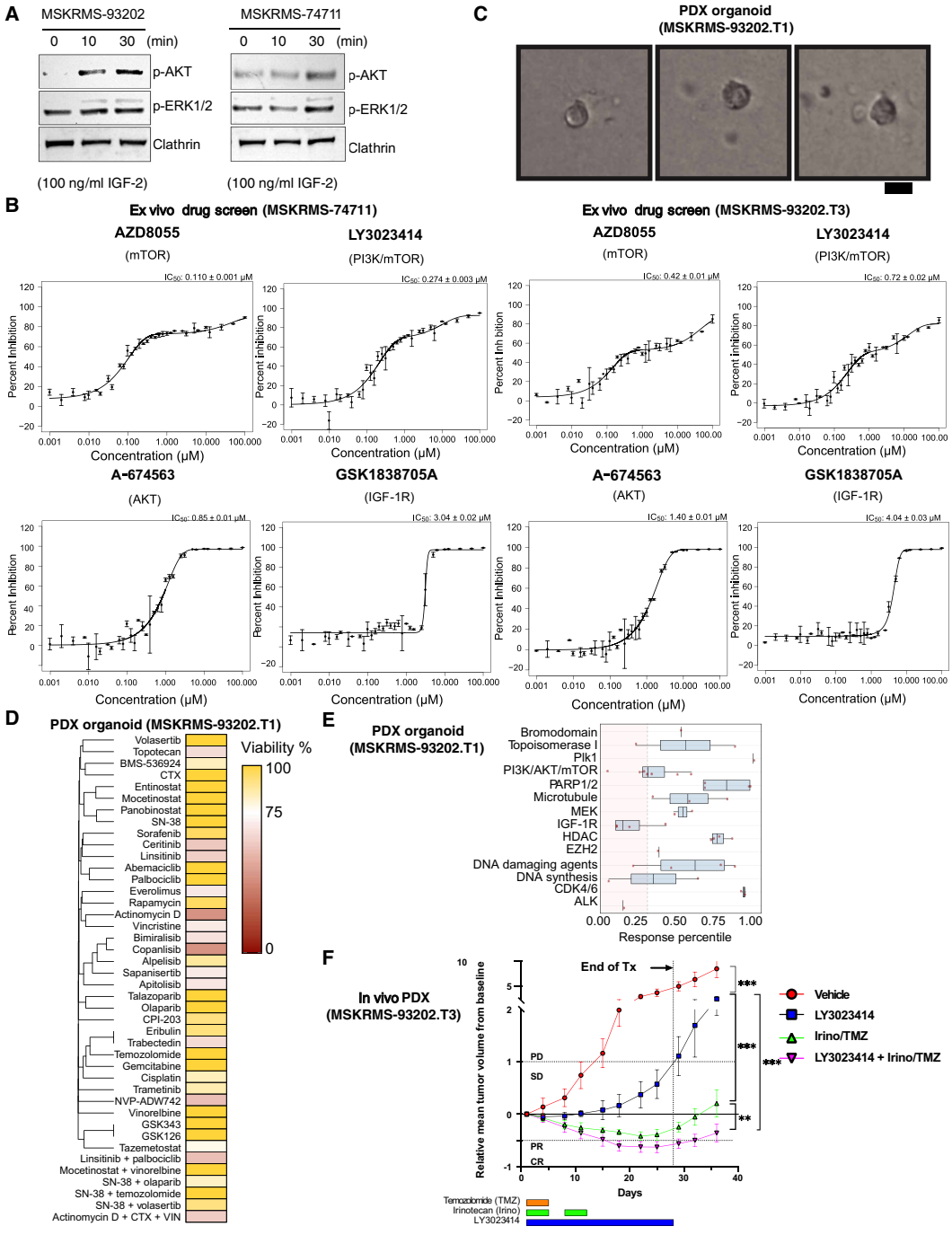

Fig. 8. Ex vivo and in vivo validation of IGF2–IGF1R–PI3K/AKT/mTOR signaling as a therapeutic dependency in *MYOD1*^{L122R}-mutant SRMS. (**A**) Immunoblot of phospho-AKT (p-AKT) and phospho-ERK1/2 (p-ERK1/2) following IGF2 stimulation in PDX-derived cell cultures. (**B**) Ex vivo drug dose response curves measuring percentage of inhibition of cell viability following 72-hour exposure to IGF1R–PI3K/AKT/mTOR pathway inhibitors in cell cultures (mean ± SD across replicates). (**C**) SRMS patient-derived tumor three-dimensional (3D) organoids (PDXOs) imaged in bright-field mode after 6 days of growth in three-dimensional (3D) Matrigel rings. Scale bar, 20 μm. (**D**) Response heatmap in a PDXO. Percentage of viability measured after a 48-hour exposure to 42 single-agent or combination regimens, each administered at 1 μM (*44*). Drugs tested as single agents are clustered by similarity in activity profiles. CTX, cyclophosphamide; VIN, vincristine. (**E**) Activity of drug classes in a mini-ring organoid screen of a PDXO. Box-and-whisker plots depict the distribution of response percentiles (0 = most potent, 1 = least potent) for compounds grouped by primary mechanism of action. Red dots represent individual compounds; boxes, center lines, and whiskers denote the interquartile range, median, and 1.5× interquartile range, respectively. The vertical dashed line and red box mark the 25th-percentile threshold, operationally defined as heightened sensitivity. (**F**) In vivo activity of a dual PI3K/mTOR inhibitor (LY3023414) in combination with chemotherapy irinotecan/temozolomide (Irino/TMZ) in a *MYOD1*^{L122R}-mutant SRMS PDX model (MSKRMS-93202.T3). Animals were randomized and treated with vehicle control, LY3023414, Irino + TMZ, or LY3023414 + Irino/TMZ ($n = 8$ mice per arm). Treatment schedules are depicted by colored horizontal bars. Treatment response thresholds for progressive disease (PD), stable disease (SD), partial response (PR), or complete response (CR) are indicated by dashed horizontal lines. Tumor volume control was compared, evaluating differences in area under tumor growth curves (AUC) and adjusting using Benjamini-Hochberg multiple testing correction. $^{**}P < 0.01$ and $^{***}P < 0.001$. Error bars: SD.

Table 2. Summary of ex vivo single agent drug sensitivity in PDX-derived disaggregated cells.

Compound	IC_{50} (μM)		Median reference IC_{50} (μM)	Description
	MSKRMS-74711	MSKRMS-93202		
Temozolomide	>100	>100	59.2	Alkylating agent
Irinotecan HCl Tihydrate	43 ± 0.3	29.5 ± 0.4	3.4	Topoisomerase I inhibitor
Everolimus	4.4 ± 0.1	9.6 ± 0.1	11.8	mTOR inhibitor
AZD8055	0.11 ± 0.001	0.42 ± 0.01	0.27	mTOR inhibitor
LY3023414	0.274 ± 0.003	0.72 ± 0.02	0.32	PI3K/mTOR inhibitor
CAL-101	49 ± 1	66 ± 2	37	PI3K δ inhibitor
LY294002	9.2 ± 0.1	18.7 ± 0.2	12.2	PI3Kα/δ/β inhibitor
MK2206 dihydrochloride	7.6 ± 0.1	11.5 ± 0.1	0.52	pan-Akt inhibitor
A-674563	0.85 ± 0.01	1.4 ± 0.01	0.96	Akt1 inhibitor
CCT128930	21.8 ± 0.2	52 ± 1	15.5	Akt2 inhibitor
BMS-754807	14 ± 0.1	22.2 ± 0.2	18.1	IGF1R/InsR inhibitor
Linsitinib	28.2 ± 0.2	20.9 ± 0.1	24.6	IGF1R inhibitor
Picropodophyllin	>100	>100	100	IGF1R inhibitor
GSK1904529A	>100	>100	100	IGF1R/IR inhibitor
GSK1838705A	3.04 ± 0.02	4.04 ± 0.03	3.54	IGF1R inhibitor

Table 3. *MYOD1*^{L122R}-mutant SRMS patient-derived organoid drug screen.

Agent (1 mM)	Target	Viability score	Viability %
Ceritinib	ALK	78.10 (6/18)	56.41
Copanlisib	PI3K	81.03 (18/50)	37.94
Linsitinib	IGF1R	82.91 (36/122)	67.62
Linsitinib + palbocilcib	IGF1R + CDK4	86.25 (6/20)	56.02
Sapanisertib	mTORC1/2	81.78 (28/76)	50.52

activity relative to vehicle control. Notably, the triple combination (LY + Irino + TMZ) elicited the most pronounced response, resulting in an object response with tumor regression, and superior volume control compared with both monotherapy ($P = 0.0005$) and chemotherapy alone ($P = 0.005$) (Fig. 8F). We further observed statistically significant improvements in PFS for all treatment arms relative to vehicle control ($P = 7.7 \times 10^{-5}$ for all comparisons). Although the triple combination (LY + Irino + TMZ) yielded a statistically significant improvement in PFS compared with chemotherapy alone ($P = 0.01$), the absolute difference in median survival was modest (50 versus 46 days) (fig. 7C).

Collectively, these results provide compelling in vivo evidence that *MYOD1*^{L122R}-mutant SRMS tumors are dependent on PI3K/mTOR signaling and that targeted inhibition of this axis can potentiate the efficacy of cytotoxic chemotherapy. These findings establish a translational rationale for combining PI3K/mTOR inhibitors with chemotherapy in this aggressive sarcoma subtype. Moreover, the identification of additional orthogonal, state-specific dependencies—such as PTK2, SYK, and LYN within the progenitor compartment—highlights potential avenues for future rational combination strategies targeting residual, potentially resistant populations, which will be evaluated in future studies.

DISCUSSION

MYOD1^{L122R}-mutant SRMS is a rare, highly aggressive sarcoma of skeletal muscle differentiation that disproportionately affects pediatric and young adult patients. It is characterized by resistance to conventional chemotherapy and dismal outcomes. While the defining *MYOD1*^{L122R} mutation is known to disrupt normal myogenic differentiation (*5*, *6*), the transcriptional architecture and regulatory mechanisms that sustain tumor growth and therapeutic resistance have remained poorly understood.

Here, we leveraged an extensively validated framework for single-cell regulatory network analysis (*22*, *23*) to systematically dissect the transcriptional heterogeneity and non-oncogene dependencies in *MYOD1*^{L122R}-mutant SRMS. This approach enables mechanistically driven inference of regulatory protein activity from sparse single-cell gene expression data by computing enrichment of a protein's target genes (*24*, *25*) using gene regulatory networks reconstructed de novo by ARACNe-AP, which are enriched for physical protein-target interactions (*26*, *27*). This allows robust detection of context-specific MR proteins defining tumor cell states and identification of actionable MR dependencies through the OncoTarget precision oncology platform (*20*, *23*, *29*)—even for genes with undetected transcripts and in the absence of targetable genetic mutations. While

recent large-scale, single-cell studies have elegantly mapped developmental hierarchies across FN- and FP-RMS (*13*–*15*), they have not systematically interrogated therapeutic vulnerabilities, and *MYOD1*^{L122R}-mutant SRMS, due to their rarity, have largely been excluded. Our regulatory network–based analysis not only defines a partially divergent transcriptional hierarchy in *MYOD1*^{L122R}-mutant SRMS but also uncovers mechanistically validated regulatory dependencies with immediate translational potential—highlighting the power of this framework to drive biological and therapeutic discovery, particularly in rare tumors with nontargetable driver mutations and few actionable coalterations.

Our analysis revealed a *MYOD1*^{L122R}-driven myogenic differentiation hierarchy in *MYOD1*^{L122R}-mutant SRMS—comprising progenitor, transition, and differentiated states—which parallels the developmental continuum observed in other RMS subtypes, yet exhibits a transcriptionally rewired progenitor-like population conserved across patient tumors and PDX models. These cell states were defined by distinct MR programs at the intersection of RMS oncogenesis and skeletal muscle development. Notably, MYOD1 activity was relatively enriched in the progenitor state, in contrast to its broad expression across early and late myogenesis in normal muscle and its relatively higher activity in differentiated FP/FN-RMS states (*15*). This suggests that the *MYOD1*^{L122R} mutation not only blocks canonical myogenic differentiation but also rewires MYOD1-driven transcriptional regulation to enforce a mesenchymal progenitor-like state characterized by high IGF2 activity and loss of downstream myogenic regulator activity. This interpretation is supported by comparative regulon analysis showing that MYOD1^{L122R} and MYOD1^{WT} engage largely distinct target gene programs, with the mutant regulon enriched for proliferative and biosynthetic pathways rather than myogenic differentiation. This progenitor state was transcriptionally distinct from previously published RMS progenitor programs (*15*), which correspond more closely to the *MYOD1*^{L122R}-mutant SRMS transition state, supporting further study of *MYOD1*^{L122R}-mutant SRMS as a molecularly unique entity with variant developmental hierarchies. Collectively, this analysis highlights how network-based regulatory inference can refine cross-subtype comparisons and supports the broader application of protein activity–based analyses to further resolve shared and divergent myogenic trajectories across RMS subtypes.

Although the transition and differentiated states partially recapitulated transcriptional features of terminal myogenesis—including enrichment in the differentiated state of a myocyte gene signature and previously described RMS "differentiated" gene programs (*13*–*16*)—they demonstrated decreased activity of MYOD1 and key downstream myogenic regulators. This suggests alternative, partially differentiated trajectories sustained either by MYOD1-independent mechanisms or occasional escape from the block imposed by the mutant protein. While this may permit some cytodifferentiation, consistent with histologic findings in some posttreatment specimens, it reflects the overall undifferentiated nature of these tumors. This is further supported by the single *MYOD1*^{L122R}-mutant SRMS sample profiled in larger RMS cohorts, found to be primarily composed of *MYOD1*^{L122R}-mutant SRMS transition and differentiated cells, showing an exceptionally low muscle lineage score (*15*).

A key insight of this study is the discovery of a paracrine signaling axis from MYOD1-high progenitor cells to IGF1R–expressing transition and differentiated states, mediated by IGF2. While IGF2 typically promotes myogenic differentiation through MYOD1 and PI3K/AKT signaling (*39*–*42*), we propose that in the context of the *MYOD1*^{L122R} mutation, IGF2 instead reinforces proliferation and survival of downstream states via IGF1R–PI3K/AKT/mTOR activation. This model is supported by differential expression and VIPER-inferred protein activity of IGF2, IGF1R, and downstream pathway components; ligand-receptor analysis; and functional validation of IGF2 ligand–dependent AKT and ERK phosphorylation in *MYOD1*^{L122R}-mutant SRMS PDX-derived cell cultures. These findings add to a growing body of evidence implicating paracrine tumor-tumor signaling in maintaining cellular hierarchies and therapeutic resistance across diverse tumor types (*49*–*52*). Our findings extend this paradigm to *MYOD1*^{L122R}-mutant SRMS and suggest that progenitor-derived IGF2 may promote survival and maintenance of the more differentiated tumor compartments.

To translate these findings, we leveraged the OncoTarget precision oncology platform (*20*) to identify cell state–specific actionable MRs for therapeutic targeting. We found conserved activation of IGF1R–PI3K/AKT/mTOR pathway components, particularly in the transition and differentiated cell states, as well as in an expanded cohort of patient and PDX *MYOD1*^{L122R}-mutant SRMS tumors profiled by bulk RNA-seq. Genomic profiling across 20 patients further revealed mutually exclusive, recurrent *IGF2* amplifications and PI3K/AKT pathway mutations in subsets of patients, consistent with previous reports of secondary PI3K/AKT pathway mutations in *MYOD1*^{L122R}-mutant SRMS (*2*–*4*, *11*, *12*). While this supports oncogenic activation of this pathway, our analysis suggests convergence of these upstream mutational patterns on shared transcriptional regulatory programs across all patients. The presence of pathway alterations may further reinforce these core transcriptional oncogenic programs, and their enrichment in posttreatment samples suggests their possible selection under therapeutic pressure, requiring further study.

We validated sensitivity to IGF1R–PI3K/AKT/mTOR high-affinity inhibitors in *MYOD1*^{L122R}-mutant SRMS PDX-derived cell cultures, 3D tumor organoids, and an in vivo PDX model—even in tumors lacking pathway mutations—suggesting a transcriptionally encoded, non-oncogene dependency on this signaling axis. This expands on prior studies validating PI3K/AKT/mTOR targeting in *MYOD1*^{L122R}-mutant SRMS tumors with co-occurring PI3K/AKT mutations (*11*, *12*), suggesting that this therapeutic approach may be more broadly relevant to this class of tumors independent of mutational status. Furthermore, we hypothesize that this paracrine signaling axis, along with IGF2-PI3K/AKT genomic alterations seen in posttreatment tumors, may represent a mechanism driving chemotherapy resistance, and provide in vivo evidence that combining PI3K/mTOR inhibitors with chemotherapy may be an effective therapeutic approach. Notably, the progenitor cell state exhibits unique actionable MRs (e.g., PTK2, SYK, LYN, and ALK), and these orthogonal dependencies may further contribute to therapy resistance. This may account for the observed in vivo tumor growth upon completion of treatment with the PI3K/mTOR inhibitor and chemotherapy. Thus, rational targeting of both the paracrine signaling axis and the progenitor state may be required to fully suppress tumor growth and overcome treatment resistance. These strategies are now being explored, including ongoing in vivo work in the well-characterized *MYOD1*^{L122R}-mutant SRMS PDX models shown to harbor the same cellular architecture and oncogenic MR vulnerabilities.

Although the genetic drivers in *MYOD1*^{L122R}-mutant SRMS have been described, to our knowledge, this study represents the most comprehensive transcriptional and regulatory atlas of *MYOD1*^{L122R}-mutant

SRMS to date, comparable in scale to single-cell studies in broader RMS cohorts (*13*–*16*). Our analysis reveals that *MYOD1*^{L122R}-mutant SRMS aligns along the broader myogenic differentiation continuum observed across RMS subtypes but features a transcriptionally rewired progenitor-like compartment, enriched in mutant MYOD1 activity. It is sustained by IGF2 paracrine signaling and is marked by distinct, targetable vulnerabilities across coexisting tumor cell states. Functionally, we demonstrate that the IGF2–IGF1R–PI3K/AKT/mTOR axis is a therapeutically relevant, mutation-independent dependency that may be leveraged, including to potentially overcome chemotherapy resistance.

While promising, this study has several limitations that will be addressed in future work. The cohort size is small and clinically heterogeneous, encompassing samples obtained at varying time points, from anatomically distinct sites, and following different treatment regimens and extents of local control. These factors preclude meaningful outcome-stratified analyses such as comparisons of cell state composition or transcriptional regulators between tumors from patients who remain alive as compared to those who experienced disease recurrence. The patient cohort is also enriched for posttreatment samples, limiting our ability to assess treatment-naïve transcriptional programs, cell state evolution under therapeutic pressure, and the relationship between cell states and treatment response or outcomes. A rigorous analysis linking tumor cell states or regulatory programs to therapy response and survival will require an expanded cohort with standardized clinical annotation, matched pre-/posttreatment or primary/relapse specimens, and longer longitudinal follow-up. Furthermore, we infer—but do not yet directly validate the cell-cell interactions involved in the paracrine IGF2–IGF1R signaling axis. Similarly, multiplex immunohistochemistry to validate the spatial coexistence of the three cell states would be informative but is challenging, as these states are defined by coordinated activity of multiple regulatory proteins, many of which lack reliable antibodies for direct detection. Future studies, including perturbational and spatially resolved approaches, will be essential to resolve the physical and functional relationships among the cell states. Furthermore, while our analysis focused on the malignant compartment given its predominance in our dataset, we acknowledge that tumor-microenvironment interactions, including those with immune and stromal cells, critically affect tumor biology and therapy response. Future studies leveraging the nontumor snRNA-seq data and complementary spatial profiling approaches will be valuable to elucidate these interactions. Last, although we identify compelling druggable MRs including in vivo validation of PI3K/mTOR inhibition, further preclinical studies in an expanded cohort, including rational combination approaches, are still needed to optimize clinical translation.

This work contributes to a growing literature supporting regulatory network analysis as a powerful approach for uncovering nonmutational therapeutic dependencies in aggressive, treatment-resistant cancers (*20*–*23*). This strategy is generalizable to other rare, heterogeneous malignancies with limited genomic drivers but substantial transcriptional complexity. Broader application of this framework may allow discovery of tractable therapeutic targets and, for example, could be extended more broadly across other high-risk RMS subtypes to better characterize common and divergent transcriptional programs and therapeutic targets for clinical translation.

In conclusion, this study defines the cell state architecture and regulatory drivers of *MYOD1*^{L122R}-mutant SRMS, identifies paracrine IGF2 signaling as a regulator of tumor progression via IGF1R-PI3K/AKT/mTOR signaling, and validates components of this axis as actionable vulnerabilities. These findings provide a mechanistic rationale and preclinical evidence supporting therapeutic targeting of the IGF1R–PI3K/AKT/mTOR pathway in this disease, nominate additional cell state–specific MR dependencies for further validation, and lay the groundwork for a precision therapy approach in an otherwise treatment-refractory sarcoma. More broadly, we illustrate the power of single-cell regulatory network analysis to uncover functional hierarchies and therapeutic opportunities in rare, transcriptionally complex tumors.

MATERIALS AND METHODS

snRNA-seq and gene expression analysis

snRNA-seq of MYOD1^{L122R}*-mutant SRMS*

Primary and relapsed snap-frozen tumor specimens from six patients with *MYOD1*^{L122R}-mutant SRMS were profiled using snRNA-seq on the 10x Genomics Chromium platform. The SRMS cases were diagnosed at the Department of Pathology and Laboratory Medicine, Memorial Sloan Kettering Cancer Center, after histopathology review of tissue specimens and confirmation of *MYOD1* L122R point mutation by Sanger sequencing or DNA sequencing by MSK-IMPACT (see below). Tissue dissociation and nucleus isolation were performed using the Singulator 100 device and citric acid–based preservation. Isolated nuclei were washed in wash buffer containing ribonuclease inhibitor (0.5 U/μl) and stained with 7-aminoactinomycin D (7-AAD) (2 μg/ml) for fluorescence-activated cell sorting. Library preparation was performed according to the manufacturer's instructions (Chromium Single Cell 3′ v2 chemistry, 10x Genomics). Briefly, polyadenylate RNA from the nuclear lysate was reverse transcribed to cDNA containing the Illumina R1 primer sequence, a unique molecular identifier, and a 10x cell barcode. The pooled barcoded cDNA was purified with Silane Dynabeads and polymerase chain reaction amplified. Appropriately sized fragments were selected for subsequent library construction. Final libraries were constructed with addition of Illumina R2 sequencing primers, paired-end adapters (P5 and P7 sequences), and sample indices. Libraries were sequenced, and raw data were processed (i.e., demultiplexing, barcode processing, gene counting, and aggregation) using the Cell Ranger software v2.1.1. FASTQ files were aligned to the human hg38 reference genome (10x Genomics; version 3.0.0).

Downstream analysis was performed in R using Seurat v5. Raw count matrices (matrix.mtx, features.tsv, and barcodes.tsv) generated by Cell Ranger were imported, and low-quality nuclei were removed. Specifically, nuclei expressing fewer than 200 genes and genes detected in fewer than three nuclei were filtered out. Noncoding genes (e.g., long noncoding RNAs and ribosomal RNA) were also removed.

Identification of malignant nuclei

Broad cell types to distinguish tumor from nontumor cells were first assigned in each sample by annotating each single cell using SingleR with the BlueprintEncodeData reference from the celldex package (*32*), which includes major immune and stromal cell types (e.g., CD4$^+$ T cells, CD8$^+$ T cells, B cells, natural killer cells, neutrophils, erythrocytes, dendritic cells (DC), monocytes, macrophages, and endothelial cells). These annotations were then used as input for InferCNV analysis (*31*) done on each sample using the respective immune cell populations as the normal reference. Malignant cells exhibiting large-scale copy number alterations were identified, and all nontumor nuclei were removed from each sample.

Gene expression analysis

Gene expression data for each sample were normalized and scaled using the Seurat SCTransform function. Samples were subsequently integrated using Seurat's anchor-based integration workflow (FindIntegrationAnchors and IntegrateData functions) to correct for technical batch effects across patients. The integrated *MYOD1*^{L122R}-mutant SRMS snRNA-seq dataset of 189,250 high-quality nuclei (177,051 malignant nuclei) was projected onto their top 10 principal components, determined by the elbow method, using the RunPCA function, and visualized in 2D space using the RunUMAP function (Fig. 1A and fig. S1B). To evaluate the effectiveness of batch correction, we generated uniform manifold approximation and projection (UMAP) plots of the complete dataset (tumor and nontumor nuclei) before and after integration, color coded by sample of origin and by tumor versus nontumor identity (fig. S1B). Before batch correction, sample-specific clustering was most pronounced within the tumor compartment and, although partially reduced, remained detectable after correction, whereas nontumor populations integrated completely. This pattern suggests that residual separation among tumor cells likely reflects biologically meaningful variation—including underlying genomic and copy-number differences, tumor site, and treatment exposure—rather than purely technical artifacts. Because excessive batch correction can overcorrect and obscure true tumor-intrinsic heterogeneity, we thus used the integrated dataset solely for visualization purposes (as in Fig. 1A) and not for downstream analyses that influence biological interpretation.

Resolution-optimized Louvain clustering

Unsupervised clustering on gene expression and subsequently on protein activity (see below) was performed by the resolution-optimized Louvain clustering algorithm (*22*). Briefly, we used the FindNeighbors and FindClusters functions in Seurat to implement the Louvain clustering algorithm. However, the FindClusters function includes a resolution parameter that modulates the final number of clusters, and investigator evaluation of ideal clustering purity is subjective. To address this, we optimized the resolution parameter objectively based on the average silhouette score (SS) width, a measure of the validity of a clustering solution. Hence, clustering was performed with resolution parameters ranging from 0.01 to 1.0 at intervals of 0.01 in random subsamples of 1000 cells over 100 iterations. The resolution parameter that maximized the mean SS across iterations was selected as the optimal resolution at which to cluster the data.

Assessment of cellular differentiation potential and cell-to-cell interactions

CytoTRACE (*34*) was performed on the integrated SCTransform count matrix to assign each nucleus a differentiation score from 0 (most differentiated) to 1 (least differentiated). For each gene, a Pearson correlation coefficient was computed to quantify its association with CytoTRACE scores across all cells, generating a numeric vector representing the gene's relationship to cellular differentiation potential. To investigate cell-cell communication, CellChat v2 (*45*) was applied to the filtered Seurat objects to infer ligand-receptor interactions and signaling pathway networks within each individual sample.

Regulatory network–based inference of single-cell protein activity by ARACNe and VIPER

MYOD1^{L122R}-mutant SRMS single-cell regulatory networks

Sample-specific *MYOD1*^{L122R}-mutant SRMS tumor gene regulatory networks—consisting of bivariate transcriptional regulatory interactions between a set of predefined putative transcriptional regulators and potential transcriptional targets—were constructed from sample-specific tumor cell gene expression profiles by the ARACNe-AP algorithm (Fig. 2) (*26*, *27*). Specifically, raw gene expression counts from cells belonging to the tumor compartment in each sample were normalized to counts per million (CPM), and $\log_2(\text{CPM} + 1)$ counts were input into the ARACNe-AP algorithm for each of the six samples independently. Candidate transcriptional regulators included 1813 transcription factors [genes annotated in the Gene Ontology (GO) Molecular Function database as GO:0003700 ("DNA binding transcription factor activity") or as GO:0003677 ("DNA binding") and GO:0030528 ("transcription regulator activity") or as GO:0003677 and GO:0045449 ("regulation of transcription")]; 969 transcriptional cofactors [a manually curated list, not overlapping with the transcription factor list, built upon genes annotated as GO:0003712 ("transcription cofactor activity") or GO:0030528 or GO:0045449]; or 3370 signaling-pathway–related genes [annotated in the GO Biological Process database as GO:0007165 ("signal transduction") and in the GO Cellular Component database as GO:0005622 ("intracellular") or GO:0005886 ("plasma membrane")]. Standard parameters were set including zero data processing inequality tolerance and mutual information *P* value threshold of 10^{-8}, computed by permutating the original dataset as a null model, consolidating 100 individual bootstraps. The resulting gene regulatory networks contained 2520 unique regulators, 5686 targets, and 366,060 interactions.

Gene expression profiles from previously published sc/snRNA-seq data were downloaded from FigShare (https://figshare.com/projects/RMS_consensus_analysis/194417) from primary patient-derived tumors: FP-RMS (SJRHB010468_D1, SJRHB013757_D2, SJRHB013759_A1, SJRHB013759_A2, SJRHB031320_D1, and SJRHB046156_R1) and *MYOD1* wild-type FN-RMS (SJRHB000026_R2, SJRHB010927_D1, SJRHB011_D, SJRHB012_R, SJRHB013758_D1, and SJRHB049189_D1) (*13*). These Seurat objects were preprocessed and contained only malignant nuclei and were downsampled to 1500 cells per sample, as previously described (*13*). Raw gene expression counts were normalized to CPM, and $\log_2(\text{CPM} + 1)$ counts were input into the ARACNe-AP algorithm for each of the above samples independently, using the same transcriptional regulator lists with the same standard parameters and consolidating 100 individual bootstraps as described above for the *MYOD1*^{L122R}-mutant SRMS dataset. The resulting gene regulatory networks from FP-RMS contained 3255 unique regulators, 9764 targets, and 585,429 interactions. The resulting gene regulatory networks from *MYOD1* wild-type FN-RMS contained 2463 unique regulators, 8408 targets, and 452,650 interactions.

Single-cell regulatory protein activity inference

Single-cell protein activity was computed for the tumor cells in each sample on the SCTransform-scaled gene expression signatures (i.e., *z*-score transformation of the SCTransform-normalized counts for each tumor nucleus scaled to the centroid of all tumor nuclei in that sample) by the metaVIPER (*25*) function in the VIPER package [Bioconductor (*24*)]. Briefly, metaVIPER adapts VIPER to single-cell data by integrating multiple gene regulatory networks on a protein-by-protein basis, weighting each network according to the square of its normalized enrichment score (NES) to emphasize those producing stronger NES values and thus more closely matching the given biological context. We computed metaVIPER-inferred protein activity on a sample-by-sample basis, interrogating the six patient-specific tumor single-cell ARACNe-AP networks to infer the activity of each transcriptional regulator based on the enrichment of its top 100 target genes in the internally scaled tumor differential

gene expression signature. This approach mitigates technical noise and patient-specific variability inherent to single-cell data, particularly in the tumor compartment, by avoiding sample integration—which may obscure biologically meaningful variation—while leveraging interpatient heterogeneity to strengthen regulatory inference across diverse transcriptional states. This yielded protein activity profiles for 2336 transcriptional regulators across the 177,051 malignant nuclei, derived from gene expression signatures of 17,828 genes (tables S3 and S4). The VIPER protein activity matrices for each sample were then loaded into a Seurat object with CreateSeuratObject, projected onto their first five principal components, determined by the elbow method, using the RunPCA function, and further reduced into a 2D visualization space using the RunUMAP function.

Similarly, for previously published FP-RMS and *MYOD1* wild-type FN-RMS, single-cell protein activity was computed for the tumor cells in each sample on the SCTransform-scaled gene expression signatures using the regulatory networks derived by ARACNe from the same samples by metaVIPER on a sample-by-sample basis. This yielded protein activity profiles for 3255 and 2463 transcriptional regulators across the 18,000 malignant nuclei from FP-RMS and FN-RMS, respectively. Subsequently, Stouffer-integrated protein activity signatures were computed across the cells belonging to the previously annotated cell states within this dataset: FP-RMS (progenitor, proliferative, differentiated, ground, apoptosis, and neuronal); FN-RMS [progenitor, proliferative, differentiated, ground, and interferon (IFN)]. We focused comparative analyses on the progenitor, proliferative, and differentiated states because they best capture the myogenic differentiation trajectory that parallels our *MYOD1*^{L122R}-mutant SRMS analysis, whereas other less lineage-related or minor states in the atlas (e.g., ground, IFN, neuronal, or apoptosis states) represented either very small cell fractions or were not lineage informative.

Identifying tumor clusters and cell states

Unsupervised clustering of the tumor single cells by VIPER-inferred protein activity for each individual sample was performed by the resolution-optimized Louvain clustering algorithm previously described, which uses the Louvain algorithm as implemented by the FindNeighbors and FindClusters functions in Seurat with the optimal resolution parameter determined by maximizing the average SS. This stratified tumor single cells into two to five clusters per sample, yielding a total of 20 sample-specific clusters across the six patients. To identify biologically meaningful cell states significantly conserved across patients, we compared the top 50 most aberrantly active MRs across each cluster, as well as cluster-specific myogenic lineage marker activity, CytoTRACE scores, and cell cycle scores. In the context of VIPER analyses, MR proteins are defined as the top 25 to 50 transcriptional regulators whose activity is most aberrantly differentially increased or decreased. Prior work has shown that the average of the top 50 most dysregulated proteins act as a concerted Tumor Checkpoint Module enforcing the cellular transcriptional phenotype and accounting for the combined effect of >80% of upstream functional mutations across tumor types (*17*, *19*, *20*, *24*).

To ensure a common reference for assessing MR similarity across clusters, we recomputed tumor single-cell metaVIPER-inferred protein activity based on a differential gene expression signature for each cell, scaled to the centroid of an equal number of randomly sampled cells from each individual cluster. We then quantified MR similarity between the mean protein activity signatures of each cluster using aREA via the viperSimilarity function in the VIPER package (*24*). This produced a distance matrix of NES scores (interpretable akin to a *z*-score), enabling identification and grouping of clusters with significantly conserved MR activity profiles into functionally relevant cell states. On the basis of unsupervised hierarchical clustering of the viperSimilarity distance matrix, the 20 subclusters were assigned to three broad groups. These were further refined by evaluating the distribution of CytoTRACE scores (see above; fig. S2B), cell proliferative fraction (fig. S2A), and myogenic lineage marker activity (fig. S2C). Specifically, if a subcluster was initially assigned to cell state 1 but had statistically significant MR overlap also to cell state 2 and if it displayed CytoTRACE and muscle lineage marker activity scores more similar to the subclusters belonging to cell state 2, then we reassigned it accordingly.

Cell cycle phase scoring was performed for each sample using Seurat's standard functions, comparing G2M and S phase scores on SCTransform-scaled gene expression data to assess proliferation differences across single cells comprising each cluster. We also evaluated enrichment of myogenic cell state lineage marker gene sets [defined in scTypeDB, https://sctype.app/database.php atlas (*53*)] in the mean protein activity signature of each subcluster by the aREA function in the VIPER package.

This integrated analysis resulted in the grouping of the 20 sample-specific subclusters into three biologically distinct cell states. Consensus cell state VIPER-inferred protein activity signatures were subsequently derived by Stouffer integration of the mean protein activity signatures of the subclusters comprising each state.

Assessment of sample contribution and robustness of VIPER-inferred cell state signatures

To evaluate whether any individual sample disproportionately influenced the inferred consensus cell state protein activity signatures, we performed two complementary robustness analyses. First, to control for potential imbalance in cell numbers between samples and states, we randomly selected an equal number of cells ($n = 2000$) from each sample × cell state combination and reran metaVIPER on each sample-specific gene expression signature using the six single-cell ARACNe networks. Consensus cell state signatures were then rederived by Stouffer integration of the mean subcluster-specific VIPER signatures within each state and compared to the corresponding consensus signatures generated from the full dataset. The downsampled and full-dataset consensus signatures were highly concordant across all cell states (NES > 15), indicating that no individual sample or cell-number imbalance drives the inferred cell state regulatory programs. Second, to confirm that cell state MRs were conserved across samples, we computed mean VIPER-inferred protein activity signatures for each sample within each cell state and compared them by viperSimilarity. This analysis revealed statistically significant overlap of top cell state MRs within individual samples [progenitor $NES_{median} = 23.0$ (10.3 to 33.6), transition $NES_{median} = 22.1$ (15.0 to 34.5), and differentiated $NES_{median} = 23.7$ (7.9 to 42.6)], further confirming that cell state MRs were consistent across tumors. Together, these analyses demonstrate that the reported cell state MR programs are robust to intersample variability, sample size imbalance, and intrinsic biological heterogeneity. Per-sample consensus cell state VIPER-inferred protein activities are provided in table S4.

snRNA-seq profiling of MYOD1^{L122R}*-mutant SRMS PDX tumors*

PDX sample from MSK-93202 (RMS211.2) was profiled using snRNA-seq on the 10x Genomics Chromium platform following the same procedures as primary patient-derived specimens. Mouse nuclei derived from stromal cells (fibroblasts and endothelial cells) are filtered

out via SingleR annotation. Following initial data processing and selection of malignant nuclei by Seurat and InferCNV, normalization and protein activity inference were performed using the aforementioned patient-derived gene regulatory network by metaVIPER. Resolution-optimized Louvain clustering was performed and cell states assigned to each cluster on the basis of which human cell state each cluster most significantly matched by viperSimilarity. Similar data processing was performed for "MSKRMS-74711" (PDX) and "29806" (primary patient sample), downloaded from GSE195709.

Identification of oncogenic MRs driving the normal-to-tumor cell state transition

To nominate cell state–specific oncogenic MRs, we obtained scRNA-seq profiles of normal human skeletal muscle from the Tabula Sapiens atlas (*47*), accessed via the CELLxGENE portal (*54*). Tumor and normal muscle count matrices were normalized and transformed to $\log_2(\text{CPM} + 1)$. For each tumor nucleus, we computed a differential gene expression signature as a *z*-score scaled to the mean and SD of the normal muscle reference (table S5). We then interrogated the six patient-derived single-cell ARACNe-AP regulatory networks by metaVIPER to infer protein activity from these normal-to-tumor differential gene expression signatures. Oncogenic MRs were defined as the top 50 most aberrantly activated regulators in the mean protein activity signature for each sample-specific cluster and consolidated cell state.

Single-cell OncoTarget drug prioritization

To identify actionable targets, the metaVIPER matrix was filtered to a previously curated list of 182 transcriptional regulators with known pharmacological inhibitors (FDA approved or in clinical trials), based on the OncoTarget precision oncology platform (*20*). For each cell state, Stouffer-integrated NES scores were computed for these 182 regulators across its constituent clusters. Significance was determined using a one-tail p-norm function with Bonferroni correction for multiple hypothesis testing across proteins within each state (Bonferroni $P \leq 10^{-5}$ considered significant).

Bulk RNA-seq analysis

Regulatory network analysis by metaVIPER of a patient with MYOD1^{L122R}-mutant SRMS and PDX bulk RNA-seq

Exome-based RNA capture sequencing was performed on archived formalin-fixed, paraffin-embedded (FFPE) tumor tissue from 24 patients with *MYOD1*^{L122R}-mutant SRMS, as previously described (*55*). Raw gene expression count matrices were obtained from F. Tirode (Cancer Research Center of Lyon; data provided in table S7). Gene counts were normalized and transformed to $\log_2(\text{CPM} + 1)$. Internally scaled gene expression signatures were generated by *z*-score transformation, scaling each gene in each sample to the mean and SD of the entire dataset. We then inferred protein activity by metaVIPER on the internally scaled differential gene expression signature using the six *MYOD1*^{L122R}-mutant SRMS tumor single-cell regulatory networks. Unsupervised clustering of the 24 bulk samples by protein activity was then performed using the partition around medoids (PAM) method on the distance matrix generated by the viperSimilarity function using the top 100 MR proteins. Optimal clustering was performed using the pamk function in the fpc package, which selects the number of clusters based on optimum average silhouette width, resulting in three transcriptionally distinct groups.

To evaluate the similarity between the single-cell–derived cell states and the bulk data, we assessed enrichment of the top and bottom 50 cell state MRs in each bulk sample protein activity signature by the aREA function. We additionally compared the Stouffer-integrated protein activity signature of each of the three single-cell cell states (i.e., Stouffer-based integration of the mean NES across the sample-specific clusters belonging to each state) to the mean protein activity signature of each bulk cluster by viperSimilarity on the top 100 MRs. We additionally analyzed bulk RNA-seq data generated from four *MYOD1*^{L122R}-mutant SRMS PDX model tumors, including MSKRMS-74711, MSKRMS-93202.T1, MSKRMS-93202.T2, and MSKRMS-93202.T3 (data provided in table S6). We generated metaVIPER-inferred protein activity as described for the bulk patient tumors and assessed MR similarity between the bulk PDX protein activity profiles and the single-cell cell states by viperSimilarity as described.

Bulk OncoTarget drug prioritization

To prioritize candidate oncogenic MRs driving the normal-to-tumor state transition in the bulk profiles, we generated a differential gene expression signature of the patient and PDX CPM-normalized bulk gene expression counts relative to the centroid of the CPM-normalized normal skeletal muscle data described previously via *z*-score transformation. We then computed sample-specific oncogenic protein activity on this gene expression signature by metaVIPER using the six single-cell regulatory networks. As before, to identify actionable targets in the bulk data, we subset this metaVIPER matrix to the previously curated list of 182 directly targetable transcriptional regulators and assessed statistical significance of their oncogenic protein activity by a one-tail p-norm function with Bonferroni correction for multiple hypothesis testing across proteins within each sample (Bonferroni $P \leq 10^{-5}$ considered significant).

Targeted DNA sequencing, copy number, and mutational profiling

Somatic mutational and copy number profiling were performed using the MSK-IMPACT platform, a clinically validated, hybridization capture-based, matched tumor-normal DNA next-generation sequencing assay that targets 341 to 505 cancer-associated genes in solid tumors, as previously described (*33*). For somatic mutation calling, MSK-IMPACT uses genomic DNA extracted from FFPE tumor samples and matched normal DNA from patient peripheral blood. Whole gene copy number alterations were inferred by comparing to a diploid reference genome from a set of normal FFPE samples; coverage of targeted regions was computed using the GATK DepthOfCoverage tool (RRID: SCR_001876). Normalized coverage values from tumor samples were divided by the corresponding values in normal samples and log transformed to yield copy number log-ratio profiles. Mutations and gene-level copy number alterations were visualized and summarized using the ComplexHeatmap package in R (RRID: SCR_017270).

IGF2 stimulation and immunoblot

Recombinant IGF2 (Sigma-Aldrich, #SRP3070) was resuspended in water + 0.01% bovine serum albumin at a final concentration of 0.01 ng/ml and stored at −80°C. For IGF2 stimulation experiments, cells from MSKRMS-74711 and MSKRMS-93202 PDX-derived cell lines were plated in Dulbecco's modified Eagle's medium (DMEM) and treated with IGF2 ligand (100 ng/ml) for 0, 10, and 30 min (1×10^6 cells per condition), after which cells were harvested and subjected to protein extraction and Western blot analysis, as previously described (*56*). Antibodies were prepared as follows: phospho–IGF1Rβ Tyr$^{1135/1136}$ (Cell Signaling Technology (CST), #3024S; 1:1000),

phospho-AKT Ser^{473} (CST, #4060T; 1:2000), phospho-ERK1/2 (CST, #9102; 1:1000), ERK1/2 (CST, #9102; 1:1000), and Clathrin (BD Biosciences, #610499; 1:20,000).

Ex vivo drug screen in PDX-derived cells

The screen was performed using viably banked PDX-derived disaggregated cells for MSKRMS-74711 (MSKPED-0162) and MSKRMS-93202 (MSKPED-0031). Cells were seeded at 4000 cells per well in DMEM:F12 complete medium containing 10% fetal bovine serum (Corning, 35-015-CV), 1% Anti-anti (Atlanta Biologicals, B22110), 1% L-glutamine (Gibco, 25030-081), 1% nonessential amino acids (Gibco, 11140-050), and 10 μM Y-27632 (ROCK inhibitor) freshly added to the medium. Dose response assessments were performed by integrating three serial dose response data with peak values of 100, 10, and 1 μM via fluorescence readout (AlamarBlue). The High Control (HC) is composed of 1% dimethyl sulfoxide (DMSO), and the Low Control (LC) 1 μM "killer mix" in 1% DMSO consists of a proprietary mixture of six cytotoxic compounds. A Z factor was computed to assess the robustness of each assay representing a dimensionless parameter that ranges from 1 to <0 and is defined as: $Z = 1 - (3\sigma HC + 3\sigma LC)/|\mu HC - \mu lC|$ where σ are the SDs and μ the averages of the high (HC) and low (LC) controls. Signal inhibition induced by the compounds was expressed as a percentage and compared to high and low controls located on the assay plates, as defined as %Inhibition = [(high control average – read value)/(high control average – low control average)] × 100. Both a logistic 4-parameter model and several potential multiphasic models were fit to the data, and model selection was performed using Bayesian information criterion (BIC) minimization. Multiphase curves were fit to the data in cases where the data did not demonstrate a standard monophasic sigmoidal curve. IC_{50} values, along with their standard errors, were estimated for each model fit. The assay was performed in triplicates using a 384-well microplate format (Corning, 3764). During the screen, internal controls were included on each plate to assess performance. Z' factors above 0.7 indicated good separation between high and low controls and a robust performance. For combination drug screens, a combination matrix of 7 × 5 × 5 of LY3023414, Irino, and TMZ was performed. 7 × 5 × 5 refers to a three-drug combination, where seven concentrations were tested for drug 1 and five concentrations each for drug 2 and drug 3. SynergyFinder was used for the analysis of the drug combination data (*57*).

Ex vivo PDX-derived organoid drug screen

The screen was performed using *MYOD1*^{L122R}-mutant SRMS MSKRMS-93202 PDX to generate PDXOs using our established mini-ring configuration for facile 3D drug screening (*54*). One 96-well plate was used, testing 36 single agents and six drug combinations. Each compound was tested at 1 μM for 48 hours, a concentration and duration selected on the basis of prior optimization in sarcoma PDXO models (*48*, *58*, *59*). Percent viability was measured by adenosine 5′-triphosphate–release assay after a 48-hour exposure to 42 single-agent or combination regimens, each administered at 1 μM as per standard screen design. This dose corresponds to clinically relevant peak plasma concentrations for many agents in the panel and has been validated as an effective discovery-screening concentration across large sarcoma PDX and PDO datasets. The 48-hour exposure period was chosen to capture early cytotoxic and cytostatic responses typical of kinase inhibitors, DNA-damaging agents, and microtubule poisons included in this screen while avoiding confounding effects of prolonged incubation. This plate passed all quality control metrics as described previously (*44*). Each compound was tested in duplicate, with 10 μM staurosporine used as a positive control ($n = 4$ wells) and 1% DMSO as negative control ($n = 8$ wells). Details of sample processing, organoid generation and viability score calculation were previously described (*43*). We calculated both cell survival (viability %) and viability scores. Viability percentage is determined by comparison to control DMSO wells within the same plate. For activity of drug classes, distribution of response percentiles for compounds grouped by primary mechanism of action is computed. Compounds within each mechanistic class function as small-molecule inhibitors of the corresponding molecular targets, except for DNA damage agents. Lower percentiles indicate greater antiproliferative potency relative to the full compound set (0 = most potent, 1 = least potent). The list of screened regimens can be found in Fig. 8D and table S8.

In vivo efficacy study

Tumor efficacy studies were performed using a *MYOD1*^{L122R}-mutant SRMS PDX (MSKRMS-93202) with tumors implanted and propagated in NSG mice (the Jackson Laboratory, strain 05557). Animals were block randomized into four treatment arms ($n = 8$ mice per arm): vehicle [PTD: 30% polyethylene glycol, molecular weight 400 (v/v) + 5% Tween 80 (v/v) in 5% dextrose water], LY3023414 (samotolisib, MedChemExpress, #HY*-12513), Irino (Selleck Chemicals, #S2217) + TMZ (Selleck Chem, #S1237), and the triple combination (LY3023414 + Irino + TMZ) when TV reached ~100 mm^3. Use of clinically relevant treatment doses and schedules were as follows: LY3023414 dosed at 10 mg/kg orally (PO) twice daily (BID) for 28 days; Irino at 1.25 mg/kg intraperitoneally (IP) daily (5 days on/2 off) for 10 days total; and TMZ at 25 mg/kg IP daily for 5 days. Tumor volume was measured twice weekly using calipers and TV calculated using a modified ellipsoid formula: TV = width^2 × 0.5 (length) where width is the shortest dimension and length is the longest dimension. The study end points included TV control through day 29 (end of treatment) and PFS with progression defined at a 100% increase in TV relative to baseline. Treatment response definitions were based on TV changes relative to baseline: Progressive disease (PD) was defined as a 100% increase in TV relative to baseline, stable disease (SD) is defined as <100% increase in TV relative to baseline but ≤50% TV reduction, partial response (PR) is >50% TV reduction, and complete response (CR) is ≥95% TV reduction. Tumor volume curves were compared using the Vardi's test comparing the area under tumor growth curves (AUC). A Kaplan-Meier estimator was used to visualize survival curves, and the log-rank test was used to test for differences in PFS outcomes across treatment groups. A Benjamini-Hochberg multiple testing correction was applied for pairwise comparisons to maintain a false discovery rate of 0.05. Significance for all analyses was determined at the 0.05 level. Animal studies were conducted under barrier conditions and an Institutional Animal Care and Use Committee (IACUC)-approved protocol (#16-08-011).

Patient survival analysis

Survival analysis was visualized by Kaplan-Meier curves and performed using R packages "survminer" version 0.4.9 (RRID: SCR_021094) and "survival" version 3.2.13 (RRID: SCR_021137). Median time (in months) to disease progression was defined as the time interval between initial diagnosis (presence of tumor seen radiographically or by pathologic confirmation) and the first instance of tumor recurrence or distant metastases after initial diagnostic

biopsy. PFS was defined as time from surgery to first local recurrence or metastasis or last clinical follow-up. DSS was defined as time from diagnosis to last clinical follow-up or death caused by disease.

Supplementary Materials

The PDF file includes:
Figs. S1 to S7
Legends for tables S1 to S8

Other Supplementary Material for this manuscript includes the following:
Tables S1 to S8

REFERENCES

1. N. P. Agaram, C. L. Chen, L. Zhang, M. P. LaQuaglia, L. Wexler, C. R. Antonescu, Recurrent MYOD1 mutations in pediatric and adult sclerosing and spindle cell rhabdomyosarcomas: Evidence for a common pathogenesis. *Genes Chromosomes Cancer* **53**, 779–787 (2014).
2. S. Kohsaka, N. Shukla, N. Ameur, T. Ito, C. K. Ng, L. Wang, D. Lim, A. Marchetti, A. Viale, M. Pirun, N. D. Socci, L. X. Qin, R. Sciot, J. Bridge, S. Singer, P. Meyers, L. H. Wexler, F. G. Barr, S. Dogan, J. A. Fletcher, J. S. Reis-Filho, M. Ladanyi, A recurrent neomorphic mutation in MYOD1 defines a clinically aggressive subset of embryonal rhabdomyosarcoma associated with PI3K-AKT pathway mutations. *Nat. Genet.* **46**, 595–600 (2014).
3. N. P. Agaram, M. P. LaQuaglia, R. Alaggio, L. Zhang, Y. Fujisawa, M. Ladanyi, L. H. Wexler, C. R. Antonescu, MYOD1-mutant spindle cell and sclerosing rhabdomyosarcoma: An aggressive subtype irrespective of age. A reappraisal for molecular classification and risk stratification. *Mod. Pathol.* **32**, 27–36 (2019).
4. J. F. Shern, J. Selfe, E. Izquierdo, R. Patidar, H. C. Chou, Y. K. Song, M. E. Yohe, S. Sindiri, J. Wei, X. Wen, E. R. Rudzinski, D. A. Barkauskas, T. Lo, D. Hall, C. M. Linardic, D. Hughes, S. Jamal, M. Jenney, J. Chisholm, R. Brown, K. Jones, B. Hicks, P. Angelini, S. George, L. Chesler, M. Hubank, A. Kelsey, S. A. Gatz, S. X. Skapek, D. S. Hawkins, J. M. Shipley, J. Khan, Genomic classification and clinical outcome in rhabdomyosarcoma: A report from an international consortium. *J. Clin. Oncol.* **39**, 2859–2871 (2021).
5. D. Di Carlo, J. Chisholm, A. Kelsey, R. Alaggio, G. Bisogno, V. Minard-Colin, M. Jenney, R. Dvila Fajardo, J. H. M. Merks, J. M. Shipley, J. L. Selfe, Biological role and clinical implications of *MYOD1*^{L122R} mutation in rhabdomyosarcoma. *Cancers (Basel)* **15**, 1644 (2023).
6. M. E. Van Antwerp, D. G. Chen, C. Chang, E. V. Prochownik, A point mutation in the MyoD basic domain imparts c-Myc-like properties. *Proc. Natl. Acad. Sci. U.S.A.* **89**, 9010–9014 (1992).
7. A. S. Pappo, J. R. Anderson, W. M. Crist, M. D. Wharam, P. P. Breitfeld, D. Hawkins, R. B. Raney, R. B. Womer, D. M. Parham, S. J. Qualman, H. E. Grier, Survival after relapse in children and adolescents with rhabdomyosarcoma: A report from the Intergroup Rhabdomyosarcoma Study Group. *J. Clin. Oncol.* **17**, 3487–3493 (1999).
8. C. Chen, H. Dorado Garcia, M. Scheer, A. G. Henssen, Current and future treatment strategies for rhabdomyosarcoma. *Front. Oncol.* **9**, 1458 (2019).
9. F. Comitani, J. O. Nash, S. Cohen-Gogo, A. I. Chang, T. T. Wen, A. Maheshwari, B. Goyal, E. S. Tio, K. Tabatabaei, C. Mayoh, R. Zhao, B. Ho, L. Brunga, J. E. G. Lawrence, P. Balogh, A. M. Flanagan, S. Teichmann, A. Huang, V. Ramaswamy, J. Hitzler, J. D. Wasserman, R. A. Gladdy, B. C. Dickson, U. Tabori, M. J. Cowley, S. Behjati, D. Malkin, A. Villani, M. S. Irwin, A. Shlien, Diagnostic classification of childhood cancer using multiscale transcriptomics. *Nat. Med.* **29**, 656–666 (2023).
10. J. W. Tsai, Y. C. ChangChien, J. C. Lee, Y. C. Kao, W. S. Li, C. W. Liang, I. C. Liao, Y. M. Chang, J. C. Wang, C. F. Tsao, S. C. Yu, H. Y. Huang, The expanding morphological and genetic spectrum of MYOD1-mutant spindle cell/sclerosing rhabdomyosarcomas: A clinicopathological and molecular comparison of mutated and non-mutated cases. *Histopathology.* **74**, 933–943 (2019).
11. M. A. Ting, J. Reuther, R. Chandramohan, H. Voicu, I. Gandhi, M. Liu, N. Cortes-Santiago, J. H. Foster, J. Hicks, J. Nuchtern, S. Scollon, S. E. Plon, M. Chintagumpala, N. Rainusso, A. Roy, D. W. Parsons, Genomic analysis and preclinical xenograft model development identify potential therapeutic targets for MYOD1-mutant soft-tissue sarcoma of childhood. *J. Pathol.* **255**, 52–61 (2021).
12. F. Choo, I. Odintsov, K. Nusser, K. S. Nicholson, L. Davis, C. L. Corless, L. Stork, R. Somwar, M. Ladanyi, J. L. Davis, M. A. Davare, Functional impact and targetability of *PI3KCA*, *GNAS*, and *PTEN* mutations in a spindle cell rhabdomyosarcoma with MYOD1 L122R mutation. *Cold Spring Harb. Mol. Case Stud.* **8**, a006140 (2022).
13. S. G. Danielli, Y. Wei, M. A. Dyer, E. Stewart, H. Sheppard, M. Wachtel, B. W. Schäfer, A. G. Patel, D. M. Langenau, Single cell transcriptomic profiling identifies tumor-acquired and therapy-resistant cell states in pediatric rhabdomyosarcoma. *Nat. Commun.* **15**, 6307 (2024).
14. A. G. Patel, X. Chen, X. Huang, M. R. Clay, N. Komorova, M. J. Krasin, A. Pappo, H. Tillman, B. A. Orr, J. McEvoy, B. Gordon, K. Blankenship, C. Reilly, X. Zhou, J. L. Norrie, A. Karlstrom, J. Yu, D. Wodarz, E. Stewart, M. A. Dyer, The myogenesis program drives clonal selection and drug resistance in rhabdomyosarcoma. *Dev. Cell* **57**, 1226–1240.e8 (2022).
15. Y. Wei, Q. Qin, C. Yan, M. N. Hayes, S. P. Garcia, H. Xi, D. Do, A. H. Jin, T. C. Eng, K. M. McCarthy, A. Adhikari, M. L. Onozato, D. Spentzos, G. P. Neilsen, A. J. Iafrate, L. H. Wexler, A. D. Pyle, M. L. Suvà, F. Dela Cruz, L. Pinello, D. M. Langenau, Single-cell analysis and functional characterization uncover the stem cell hierarchies and developmental origins of rhabdomyosarcoma. *Nat. Cancer* **3**, 961–975 (2022).
16. S. G. Danielli, E. Porpiglia, A. J. De Micheli, N. Navarro, M. J. Zellinger, I. Bechtold, S. Kisele, L. Volken, J. G. Marques, S. Kasper, P. K. Bode, A. G. Henssen, D. Gürgen, O. Delattre, D. Surdez, J. Roma, P. Bühlmann, H. M. Blau, M. Wachtel, B. W. Schäfer, Single-cell profiling of alveolar rhabdomyosarcoma reveals RAS pathway inhibitors as cell-fate hijackers with therapeutic relevance. *Sci. Adv.* **9**, eade9238 (2023).
17. A. Califano, M. J. Alvarez, The recurrent architecture of tumour initiation, progression and drug sensitivity. *Nat. Rev. Cancer* **17**, 116–130 (2017).
18. A. Aytes, A. Mitrofanova, C. Lefebvre, M. J. Alvarez, M. Castillo-Martin, T. Zheng, J. A. Eastham, A. Gopalan, K. J. Pienta, M. M. Shen, A. Califano, C. Abate-Shen, Cross-species regulatory network analysis identifies a synergistic interaction between FOXM1 and CENPF that drives prostate cancer malignancy. *Cancer Cell* **25**, 638–651 (2014).
19. E. O. Paull, A. Aytes, S. J. Jones, P. S. Subramaniam, F. M. Giorgi, E. F. Douglass, S. Tagore, B. Chu, A. Vasciaveo, S. Zheng, R. Verhaak, C. Abate-Shen, M. J. Alvarez, A. Califano, A modular master regulator landscape controls cancer transcriptional identity. *Cell* **184**, 334–351.e20 (2021).
20. P. S. Mundi, M. J. Alvarez, R. Realubit, J. Y. Kim, A. Vasciaveo, A. Mitrofanova, L. Zanella, E. F. Douglass, J. M. Arriaga, N. Kim, D. D. Mulholland, D. C. Wilkes, M. W. Khan, K. Mullangi, A. Califano, A transcriptome-based precision oncology platform for patient-therapy alignment in a diverse set of treatment-resistant malignancies. *Cancer Discov.* **13**, 1386–1407 (2023).
21. A. Vasciaveo, J. M. Arriaga, F. N. de Almeida, M. Zou, E. F. Douglass, F. Picech, M. Shibata, A. Rodriguez-Calero, S. de Brot, A. Mitrofanova, C. W. Chua, C. Karan, R. Realubit, S. Pampou, J. Y. Kim, S. N. Afari, T. Mukhammadov, L. Zanella, E. Corey, M. J. Alvarez, M. A. Rubin, M. M. Shen, A. Califano, C. Abate-Shen, OncoLoop: A network-based precision cancer medicine framework. *Cancer Discov.* **13**, 386–409 (2023).
22. A. Obradovic, N. Chowdhury, S. M. Haake, C. Ager, V. Wang, L. Vlahos, X. V. Guo, D. H. Aggen, W. K. Rathmell, E. Jonasch, J. E. Johnson, M. Roth, K. E. Beckermann, B. I. Rini, J. McKiernan, A. Califano, C. G. Drake, Single-cell protein activity analysis identifies recurrence-associated renal tumor macrophages. *Cell* **184**, 2988–3005.e16 (2021).
23. E. C. Fernández, L. Tomassoni, X. Zhang, J. Wang, A. Obradovic, P. Laise, A. T. Griffin, L. Vlahos, H. E. Minns, D. V. Morales, C. Simmons, M. Gallitto, H. J. Wei, T. J. Martins, P. S. Becker, J. R. Crawford, T. Tzaridis, R. J. Wechsler-Reya, J. Garvin, R. D. Gartrell, L. Szalontay, S. Zacharoulis, C. C. Wu, Z. Zhang, A. Califano, J. Pavisic, Elucidation and pharmacologic targeting of master regulator dependencies in coexisting diffuse midline glioma subpopulations. bioRxiv 2024.03.17.585370 [Preprint] (2024). https://doi.org/10.1101/2024.03.17.585370.
24. M. J. Alvarez, Y. Shen, F. M. Giorgi, A. Lachmann, B. B. Ding, B. H. Ye, A. Califano, Functional characterization of somatic mutations in cancer using network-based inference of protein activity. *Nat. Genet.* **48**, 838–847 (2016).
25. H. Ding, E. F. Douglass Jr., A. M. Sonabend, A. Mela, S. Bose, C. Gonzalez, P. D. Canoll, P. A. Sims, M. J. Alvarez, A. Califano, Quantitative assessment of protein activity in orphan tissues and single cells using the metaVIPER algorithm. *Nat. Commun.* **9**, 1471 (2018).
26. A. A. Margolin, I. Nemenman, K. Basso, C. Wiggins, G. Stolovitzky, R. Dalla Favera, A. Califano, ARACNE: An algorithm for the reconstruction of gene regulatory networks in a mammalian cellular context. *BMC Bioinformatics* **7**, S7 (2006).
27. A. Lachmann, F. M. Giorgi, G. Lopez, A. Califano, ARACNe-AP: Gene network reverse engineering through adaptive partitioning inference of mutual information. *Bioinformatics* **32**, 2233–2235 (2016).
28. L. Vlahos, A. Obradovic, J. Worley, X. Tan, A. Howe, P. Laise, A. Wang, C. G. Drake, A. Califano, Systematic, protein activity-based characterization of single cell state. bioRxiv 2021.05.20.445002 [Preprint] (2023). https://doi.org/10.1101/2021.05.20.445002.
29. T. Z. Zeleke, Q. Pan, C. Chiuzan, M. Onishi, Y. Li, H. Tan, M. J. Alvarez, E. Honan, M. Yang, P. L. Chia, P. Mukhopadhyay, S. Kelly, R. Wu, K. Fenn, M. S. Trivedi, M. Accordino, K. D. Crew, D. L. Hershman, M. Maurer, S. Jones, A. High, J. Peng, A. Califano, K. Kalinsky, J. Yu, J. Silva, Network-based assessment of HDAC6 activity predicts preclinical and clinical responses to the HDAC6 inhibitor ricolinostat in breast cancer. *Nat. Cancer* **4**, 257–275 (2023).
30. M. J. Alvarez, P. S. Subramaniam, L. H. Tang, A. Grunn, M. Aburi, G. Rieckhof, E. V. Komissarova, E. A. Hagan, L. Bodei, P. A. Clemons, F. S. Dela Cruz, D. Dhall, D. Diolaiti, D. A. Fraker, A. Ghavami, D. Kaemmerer, C. Karan, M. Kidd, K. M. Kim, H. C. Kim, L. P. Kunju, Ü. Langel, Z. Li, J. Lee, H. Li, V. LiVolsi, R. Pfragner, A. R. Rainey, R. B. Realubit, H. Remotti, J. Regberg, R. Roses, A. Rustgi, A. R. Sepulveda, S. Serra, C. Shi, X. Yuan, M. Barberis, R. Bergamaschi, A. M. Chinnaiyan, T. Detre, S. Ezzat, A. Frilling, M. Hommann, D. Jaeger,

M. K. Kim, B. S. Knudsen, A. L. Kung, E. Leahy, D. C. Metz, J. W. Milsom, Y. S. Park, D. Reidy-Lagunes, S. Schreiber, K. Washington, B. Wiedenmann, I. Modlin, A. Califano, A precision oncology approach to the pharmacological targeting of mechanistic dependencies in neuroendocrine tumors. *Nat. Genet.* **50**, 979–989 (2018).
31. T. Tickle, I. Tirosh, C. Georgescu, M. Brown, B. Haas, "inferCNV of the Trinity CTAT Project" (Klarman Cell Observatory, Broad Institute of MIT and Harvard, Cambridge, MA, USA, 2019); https://github.com/broadinstitute/inferCNV.
32. D. Aran, A. P. Looney, L. Liu, E. Wu, V. Fong, A. Hsu, S. Chak, R. P. Naikawadi, P. J. Wolters, A. R. Abate, A. J. Butte, M. Bhattacharya, Reference-based analysis of lung single-cell sequencing reveals a transitional profibrotic macrophage. *Nat. Immunol.* **20**, 163–172 (2019).
33. D. T. Cheng, T. N. Mitchell, A. Zehir, R. H. Shah, R. Benayed, A. Syed, R. Chandramohan, Z. Y. Liu, H. H. Won, S. N. Scott, A. R. Brannon, C. O'Reilly, J. Sadowska, J. Casanova, A. Yannes, J. F. Hechtman, J. Yao, W. Song, D. S. Ross, A. Oultache, S. Dogan, L. Borsu, M. Hameed, K. Nafa, M. E. Arcila, M. Ladanyi, M. F. Berger, Memorial sloan kettering-integrated mutation profiling of actionable cancer targets (MSK-IMPACT): A hybridization capture-based next-generation sequencing clinical assay for solid tumor molecular oncology. *J. Mol. Diagn.* **17**, 251–264 (2015).
34. G. S. Gulati, S. S. Sikandar, D. J. Wesche, A. Manjunath, A. Bharadwaj, M. J. Berger, F. Ilagan, A. H. Kuo, R. W. Hsieh, S. Cai, M. Zabala, F. A. Scheeren, N. A. Lobo, D. Qian, F. B. Yu, F. M. Dirbas, M. F. Clarke, A. M. Newman, Single-cell transcriptional diversity is a hallmark of developmental potential. *Science* **24**, 405–411 (2020).
35. ENCODE Project Consortium, A user's guide to the encyclopedia of DNA elements (ENCODE). *PLoS Biol.* **9**, e1001046 (2011).
36. E. Y. Chen, C. M. Tan, Y. Kou, Q. Duan, Z. Wang, G. V. Meirelles, N. R. Clark, A. Ma'ayan, Enrichr: Interactive and collaborative HTML5 gene list enrichment analysis tool. *BMC Bioinformatics* **14**, 128 (2013).
37. M. V. Kuleshov, M. R. Jones, A. D. Rouillard, N. F. Fernandez, Q. Duan, Z. Wang, S. Koplev, S. L. Jenkins, K. M. Jagodnik, A. Lachmann, M. G. McDermott, C. D. Monteiro, G. W. Gundersen, A. Ma'ayan, Enrichr: A comprehensive gene set enrichment analysis web server 2016 update. *Nucleic Acids Res.* **44**, W90–W97 (2016).
38. Z. Xie, A. Bailey, M. V. Kuleshov, D. J. B. Clarke, J. E. Evangelista, S. L. Jenkins, A. Lachmann, M. L. Wojciechowicz, E. Kropiwnicki, K. M. Jagodnik, M. Jeon, A. Ma'ayan, Gene set knowledge discovery with Enrichr. *Curr. Protoc.* **1**, e90 (2021).
39. S. C. Bendall, M. H. Stewart, P. Menendez, D. George, K. Vijayaragavan, T. Werbowetski-Ogilvie, V. Ramos-Mejia, A. Rouleau, J. Yang, M. Bossé, G. Lajoie, M. Bhatia, IGF and FGF cooperatively establish the regulatory stem cell niche of pluripotent human cells in vitro. *Nature* **448**, 1015–1021 (2007).
40. V. Barroca, D. Lewandowski, A. Jaracz-Ros, S. N. Hardouin, Paternal insulin-like growth factor 2 (Igf2) regulates stem cell activity during adulthood. *EBioMedicine* **15**, 150–162 (2017).
41. A. Youssef, D. Aboalola, V. K. Han, The roles of insulin-like growth factors in mesenchymal stem cell niche. *Stem Cells Int.* **2017**, 9453108 (2017).
42. E. M. Wilson, M. M. Hsieh, P. Rotwein, Autocrine growth factor signaling by insulin-like growth factor-II mediates MyoD-stimulated myocyte maturation. *J. Biol. Chem.* **278**, 41109–41113 (2003).
43. E. M. Wilson, P. Rotwein, Control of MyoD function during initiation of muscle differentiation by an autocrine signaling pathway activated by insulin-like growth factor-II. *J. Biol. Chem.* **281**, 29962–29971 (2006).
44. D. T. Alzhanov, S. F. McInerney, P. Rotwein, Long range interactions regulate Igf2 gene transcription during skeletal muscle differentiation. *J. Biol. Chem.* **285**, 38969–38977 (2010).
45. S. Jin, M. V. Plikus, Q. Nie, CellChat for systematic analysis of cell-cell communication from single-cell transcriptomics. *Nat. Protoc.* **20**, 180–219 (2025).
46. J. Brown, E. Y. Jones, B. E. Forbes, Interactions of IGF-II with the IGF2R/cation-independent mannose-6-phosphate receptor mechanism and biological outcomes. *Vitam. Horm.* **80**, 699–719 (2009).
47. Tabula Sapiens Consortium, The Tabula Sapiens: A multiple-organ, single-cell transcriptomic atlas of humans. *Science* **376**, eabl4896 (2022).
48. A. Al Shihabi, P. J. Tebon, H. T. L. Nguyen, J. Chantharasamee, S. Sartini, A. Davarifar, A. Y. Jensen, M. Diaz-Infante, H. Cox, A. E. Gonzalez, S. Norris, J. Sperry, J. Nakashima, N. Tavanaie, H. Winata, S. T. Fitz-Gibbon, T. N. Yamaguchi, J. H. Jeong, S. Dry, A. S. Singh, B. Chmielowski, J. G. Crompton, A. K. Kalbasi, F. C. Eilber, F. Hornicek, N. M. Bernthal, S. D. Nelson, P. C. Boutros, N. C. Federman, J. Yanagawa, A. Soragni, The landscape of drug sensitivity and resistance in sarcoma. *Cell Stem Cell* **31**, 1524–1542.e4 (2024).
49. T. Tammela, F. J. Sanchez-Rivera, N. M. Cetinbas, K. Wu, N. S. Joshi, K. Helenius, Y. Park, R. Azimi, N. R. Kerper, R. A. Wesselhoeft, X. Gu, L. L. Schmidt, M. Cornwall-Brady, Ö. H. Yilmaz, W. Xue, P. Katajisto, A. Bhutkar, T. Jacks, A Wnt-producing niche drives proliferative potential and progression in lung adenocarcinoma. *Nature* **545**, 355–359 (2017).
50. Y. Lai, X. Lu, Y. Liao, P. Ouyang, H. Wang, X. Zhang, G. Huang, S. Qi, Y. Li, Crosstalk between glioblastoma and tumor microenvironment drives proneural-mesenchymal transition through ligand-receptor interactions. *Genes Dis.* **11**, 874–889 (2023).
51. F. Lüönd, S. Tiede, G. Christofori, Breast cancer as an example of tumour heterogeneity and tumour cell plasticity during malignant progression. *Br. J. Cancer* **125**, 164–175 (2021).
52. J. Zhang, J. Cunningham, J. Brown, R. Gatenby, Evolution-based mathematical models significantly prolong response to abiraterone in metastatic castrate-resistant prostate cancer and identify strategies to further improve outcomes. *eLife* **11**, e76284 (2022).
53. A. Ianevski, A. K. Giri, T. Aittokallio, Fully-automated and ultra-fast cell-type identification using specific marker combinations from single-cell transcriptomic data. *Nat. Commun.* **13**, 1246 (2022).
54. S. Abdulla, B. Aevermann, P. Assis, S. Badajoz, S. M. Bell, E. Bezzi, B. Cakir, J. Chaffer, S. Chambers, J. M. Cherry, T. Chi, J. Chien, L. Dorman, P. Garcia-Nieto, N. Gloria, M. Hastie, D. Hegeman, J. Hilton, T. Huang, A. Infeld, A. M. Istrate, I. Jelic, K. Katsuya, Y. J. Kim, K. Liang, M. Lin, M. Lombardo, B. Marshall, B. Martin, F. McDade, C. Megill, N. Patel, A. Predeus, B. Raymor, B. Robatmili, D. Rogers, E. Rutherford, D. Sadgat, A. Shin, C. Small, T. Smith, P. Sridharan, A. Tarashansky, N. Tavares, H. Thomas, A. Tolopko, M. Urisko, J. Yan, G. Yeretssian, J. Zamanian, A. Mani, J. Cool, A. Carr, CZ CELLxGENE Discover: A single-cell data platform for scalable exploration, analysis and modeling of aggregated data. *Nucleic Acids Res.* **53**, D886–D900 (2025).
55. N. Macagno, D. Pissaloux, A. de la Fouchardière, M. Karanian, S. Lantuejoul, F. Galateau Salle, A. Meurgey, C. Chassagne-Clement, I. Treilleux, C. Renard, J. Roussel, J. Gervasoni, V. Cockenpot, C. Crozes, A. Baltres, A. Houlier, S. Paindavoine, L. Alberti, A. Duc, F. Le Loarer, A. Dufresne, M. Brahmi, N. Corradini, J. Y. Blay, F. Tirode, Wholistic approach: Transcriptomic analysis and beyond using archival material for molecular diagnosis. *Genes Chromosomes Cancer* **61**, 382–393 (2022).
56. F. Vanoli, B. Meskauskaite, L. Herviou, W. Mallen, Y. S. Sung, Y. Fujisawa, L. Zhang, S. Simon, D. Huangfu, M. Jasin, C. R. Antonescu, Generation of human embryonic stem cell models to exploit the EWSR1-CREB fusion promiscuity as a common pathway of transformation in human tumors. *Oncogene* **40**, 5095–5104 (2021).
57. A. Ianevski, A. K. Giri, T. Aittokallio, SynergyFinder 3.0: An interactive analysis and consensus interpretation of multi-drug synergies across multiple samples. *Nucleic Acids Res.* **50**, W739–W743 (2022).
58. N. Phan, J. J. Hong, B. Tofig, M. Mapua, D. Elashoff, N. A. Moatamed, J. Huang, S. Memarzadeh, R. Damoiseaux, A. Soragni, A simple high-throughput approach identifies actionable drug sensitivities in patient-derived tumor organoids. *Commun. Biol.* **2**, 78 (2019).
59. A. Al Shihabi, A. Davarifar, H. T. L. Nguyen, N. Tavanaie, S. D. Nelson, J. Yanagawa, N. Federman, N. Bernthal, F. Hornicek, A. Soragni, Personalized chordoma organoids for drug discovery studies. *Sci. Adv.* **8**, eabl3674 (2022).

Acknowledgments

Funding: This work was funded by the National Institutes of Health grant P50 CA217694 (C.R.A.), the National Institutes of Health grant P50CA272170 (J.K.D.), the National Institutes of Health grant P30 CA008748 (C.R.A.), the National Institutes of Health grant R01CA244729 (A.Si.), the National Institutes of Health grant R01CA244729-03S (A.So.), the Cycle for Survival (C.R.A. and L.H.W.), the Kristin Ann Carr Foundation (C.R.A.), the PaulieStrong Foundation (F.S.D.C.), and Curing Kids Cancer (F.S.D.C.). **Author contributions:** Conceptualization: J.K.D., F.V., H.d.T.d.W., M.K., L.H.W., F.S.D.C., J.P., and C.R.A. Methodology: J.K.D., H.d.T.d.W., P.S., J.N.L., D.Y., M.K., A.So., F.S.D.C., J.P., and C.R.A. Data curation: J.K.D., H.d.T.d.W., D.P., M.K., and L.H.W. Validation: J.K.D., H.d.T.d.W., D.Y., M.K., L.H.W., F.S.D.C., and J.P. Resources: F.V., P.S., D.P., M.K., D.Y., F.T., L.H.W., A.K., A.So., F.S.D.C., and C.R.A. Formal analysis: J.K.D., J.N.L., S.B., M.K., A.So., F.S.D.C., and J.P. Software: J.K.D. and J.P. Investigation: J.K.D., F.V., H.d.T.d.W., G.I.S., P.S., A.Si., D.P., M.K., G.I.S., D.Y., J.N.L., A.So., and C.R.A. Visualization: J.K.D., F.V., H.d.T.d.W., G.I.S., P.S., J.N.L., G.I.S., P.S., S.B., A.So., J.P., and C.R.A. Funding acquisition: L.H.W., A.K., and C.R.A. Project administration: D.Y., F.S.D.C., J.P., and C.R.A. Supervision: A.K., F.S.D.C., J.P., and C.R.A. Writing—original draft: J.K.D., A.So., J.P., and C.R.A. Writing—review and editing: J.K.D., F.V., H.d.T.d.W., P.S., M.K., J.N.L., F.T., L.H.W., A.K., A.So., F.S.D.C., J.P., and C.R.A. **Competing interests:** The authors declare that they have no competing interests. **Data, code, and materials availability:** All data and code needed to evaluate and reproduce the conclusions in the paper are present in the paper, the Supplementary Materials, and/or open access data repositories (see below). No new materials were generated in this study. Raw sequencing and processed data from snRNA-seq are deposited and available in the NCBI Gene Omnibus (GSE accession number GSE288065). snRNA-seq barcode, matrix, and feature CellRanger output files from two additional *MYOD1*^{L122R}-mutant SRMS snRNA-seq datasets, specimens labeled MSKRMS-74711 (PDX) and 29806 (primary patient sample), were downloaded from GSE195709 (Y. Wei; 2022). Bulk RNA-seq count data are available in the Supplementary Materials. Genomic data from 20 patients with *MYOD1*^{L122R}-mutant SRMS are available from cBioPortal (www.cbioportal.org/study/summary?id=soft_tissue_myod1_msk_2025). The ARACNe algorithm is hosted permanently on https://califano.c2b2.columbia.edu/aracne. The viper R package is archived on Bioconductor (www.bioconductor.org/packages/release/bioc/html/viper.html). The source code used to generate the results reported in this manuscript is available through a GitHub repository (https://github.com/dermawaj/MYOD1snRNA) and in Zenodo at (https://doi.org/10.5281/zenodo.18636295).

Submitted 15 July 2025
Accepted 22 January 2026
Published 27 February 2026
10.1126/sciadv.aea6453

ScienceAdvances

Single-cell protein activity analysis reveals aberrant myogenesis and IGF2-PI3K pathway dependencies in *MYOD1*-mutant rhabdomyosarcoma

Josephine K. Dermawan, Fabio Vanoli, Henry de Traux de Wardin, Jonathan N. Levi, Glorymar Ibanez Sanchez, Armaan Siddiquee, Samantha Brosius, Daoqi You, Franck Tirode, Patricia Sung, Marie Karanian, Daniel Pissaloux, Leonard H. Wexler, Andrew Kung, Alice Soragni, Filemon S. Dela Cruz, Jovana Pavisic, and Cristina R. Antonescu

Sci. Adv. **12** (9), eaea6453. DOI: 10.1126/sciadv.aea6453